Supporting Information for

# Tunable Electrical Conductivity of Flexible Metal–Organic Frameworks

Sanggyu Chong[1†], Sven M. J. Rogge[2†], Jihan Kim[1*]

**1**: Department of Chemical and Biomolecular Engineering, Korea Advanced Institute of Science and Technology (KAIST), Daejeon 34141, South Korea

**2**: Center for Molecular Modeling (CMM), Ghent University, Zwijnaarde 9052, Belgium

†: These authors contributed equally to this work.

\*: Author to whom correspondence should be addressed: jihankim@kaist.ac.kr

## Table of Contents

**Figure S1.** Structure of Zn(NDIDP) in the *lp* phase (top) and *np* phase (bottom). (gray: Zn, brown: C, red: O, light blue: N, white: H)
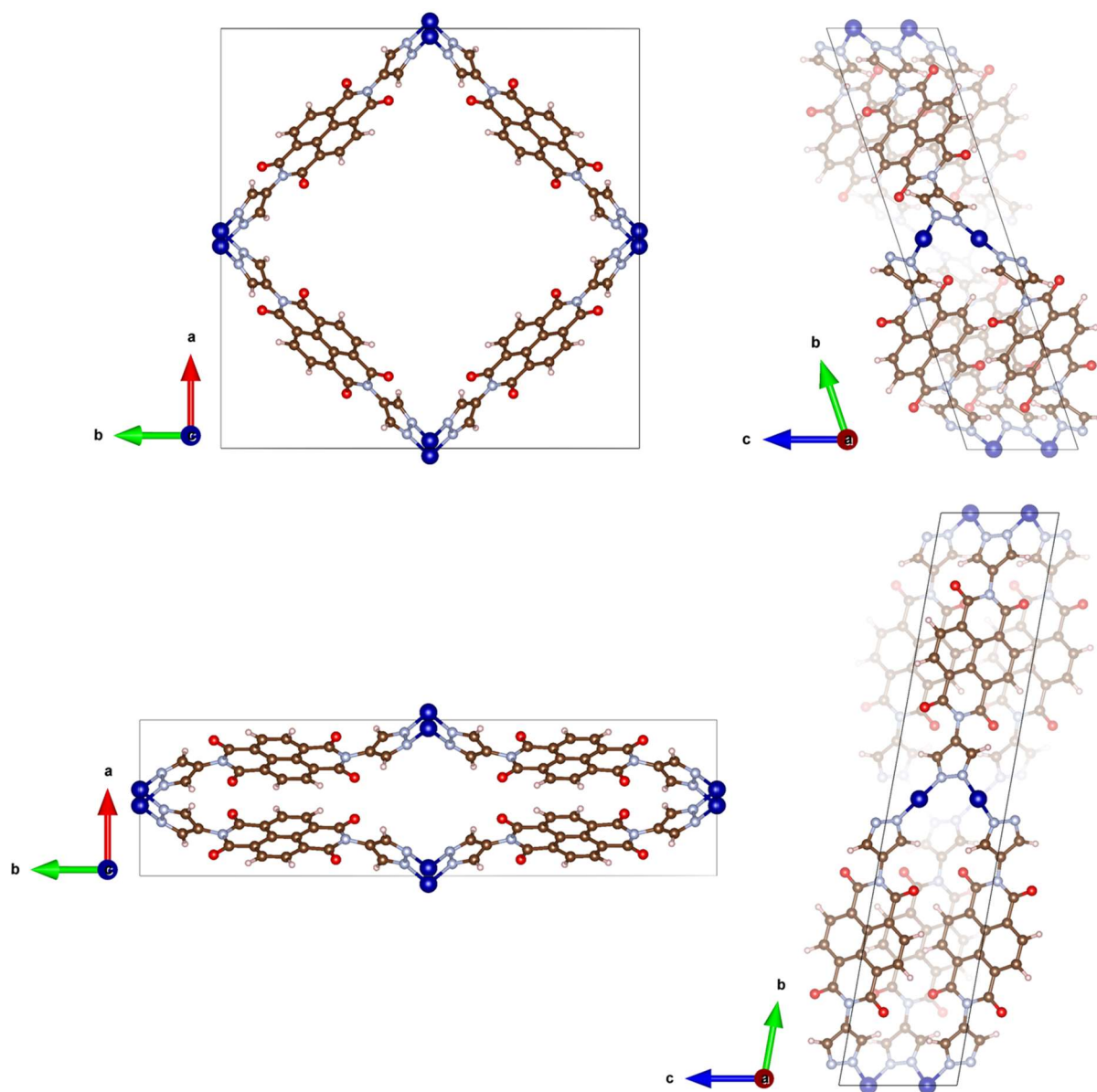
**Figure S2.** Structure of Co(NDIDP) in the *lp* phase (top) and *np* phase (bottom). (blue: Co, brown: C, red: O, light blue: N, white: H)
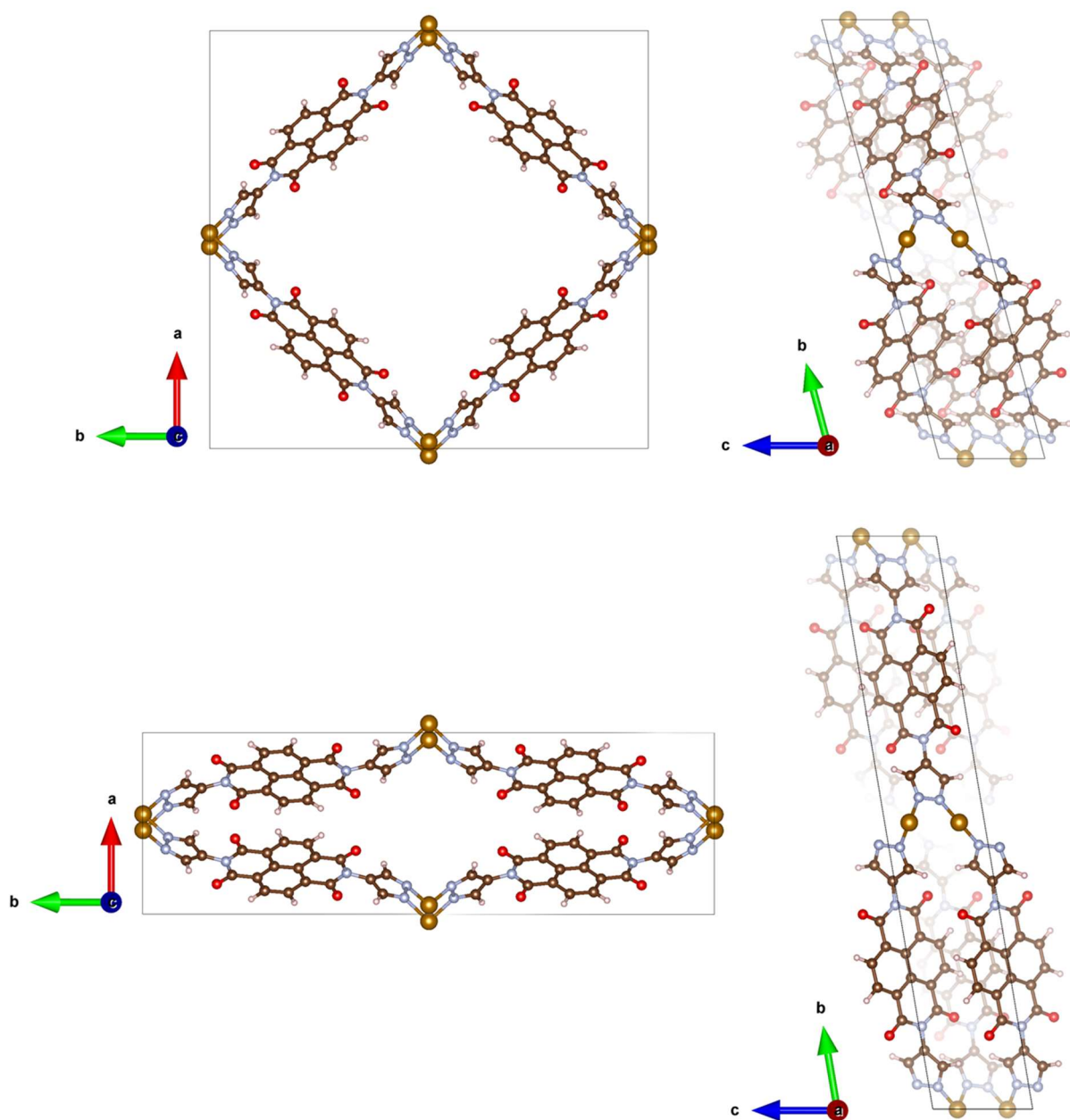
**Figure S3.** Structure of Fe(NDIDP) in the *lp* phase (top) and *np* phase (bottom). (gold: Fe, brown: C, red: O, light blue: N, white: H)
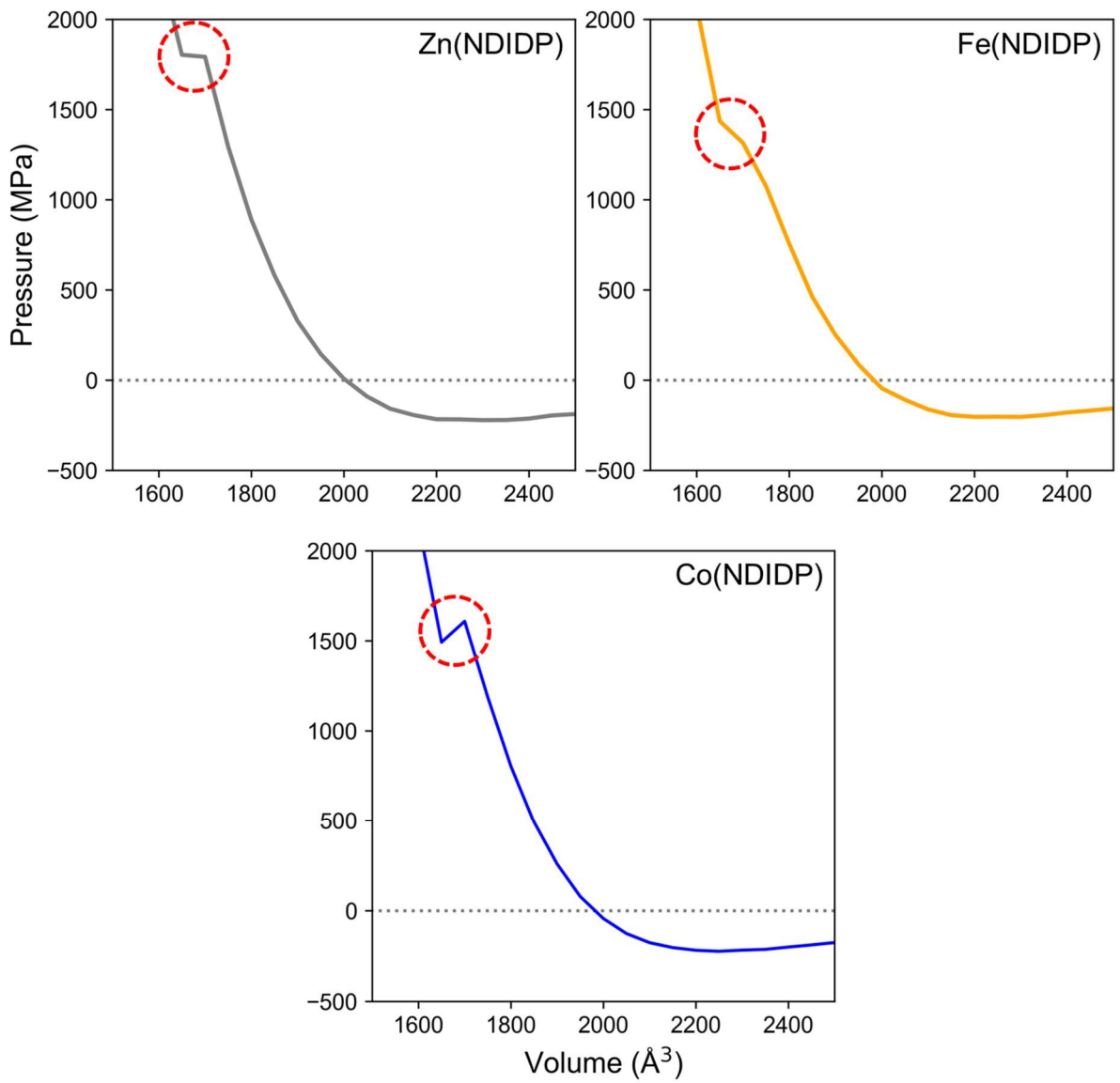
**Figure S4.** $P(V)$ equations of state at 300 K focused onto the anomalous feature of the curve found in the lower volume range for Zn(NDIDP) (top left), Fe(NDIDP) (top right), and Co(NDIDP) (bottom). Anomalies are further highlighted with red dotted circles and are discussed in the main text.
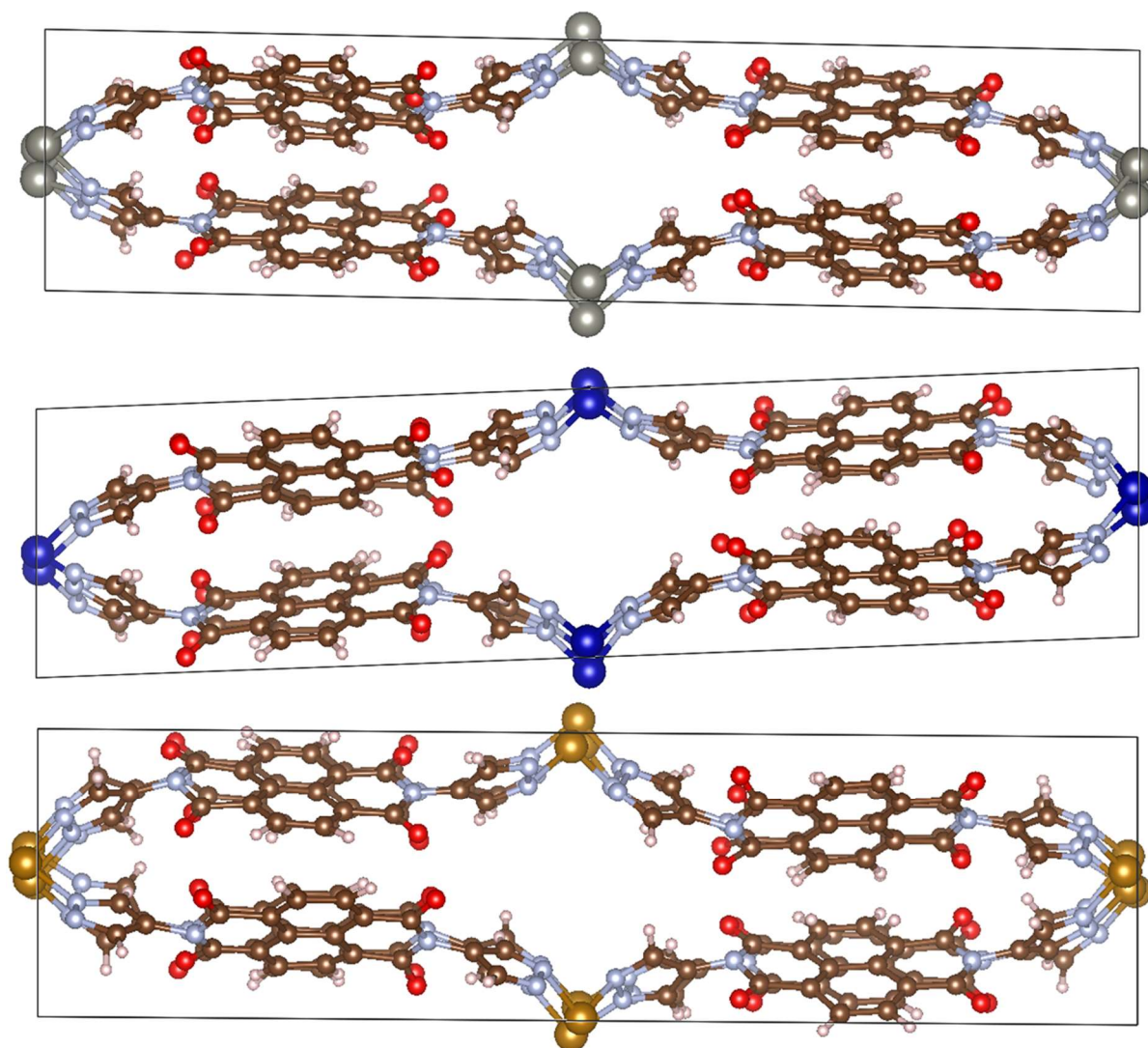
**Figure S5.** M(NDIDP) structures, viewed along the *z*-axis, as extracted from MD simulations at volumes higher than the $P(V)$ curve anomaly. (gray: Zn, blue: Co, gold: Fe, brown: C, red: O, light blue: N, white: H)
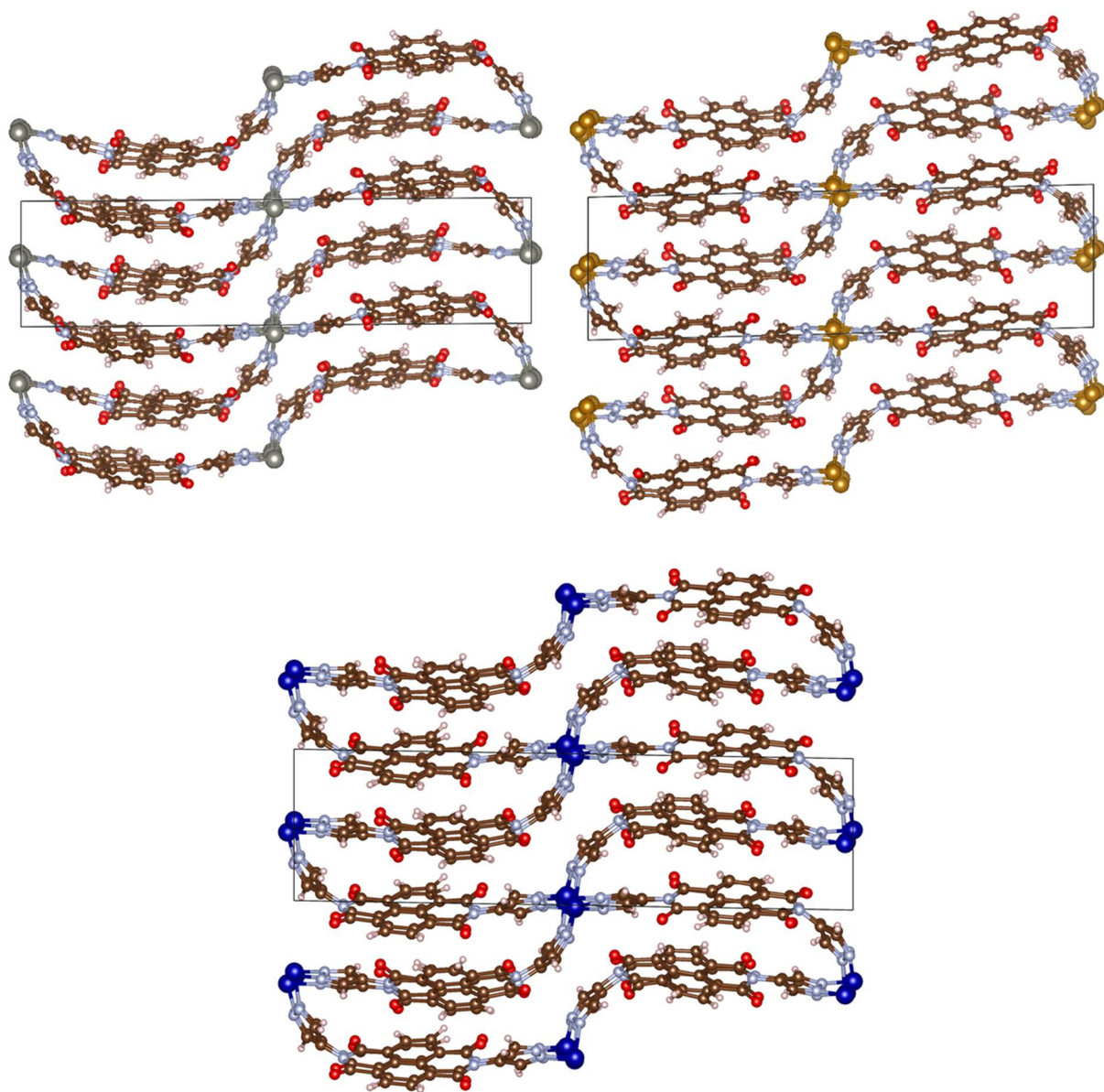
**Figure S6.** M(NDIDP) structures, viewed along the *z*-axis, as extracted from MD simulations at volumes lower than the *P*(*V*) curve anomaly. (gray: Zn, blue: Co, gold: Fe, brown: C, red: O, light blue: N, white: H)
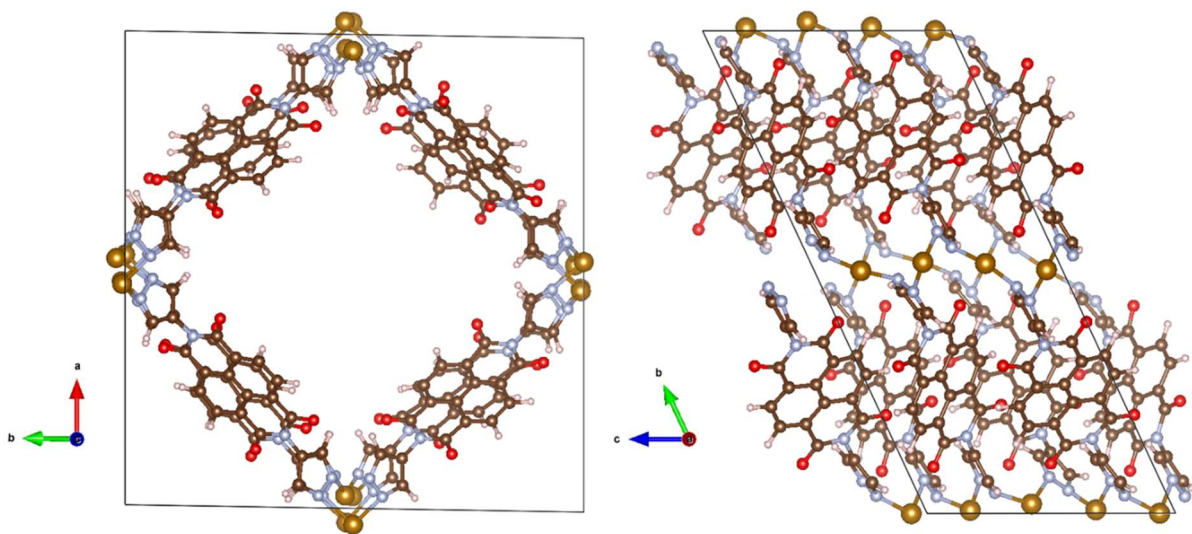
**Figure S7.** Fe(NDIDP) structures extracted from MD simulations which have fallen into the secondary phase that exhibits significant shearing of the framework in the *yz* direction. (gold: Fe, brown: C, red: O, light blue: N, white: H)
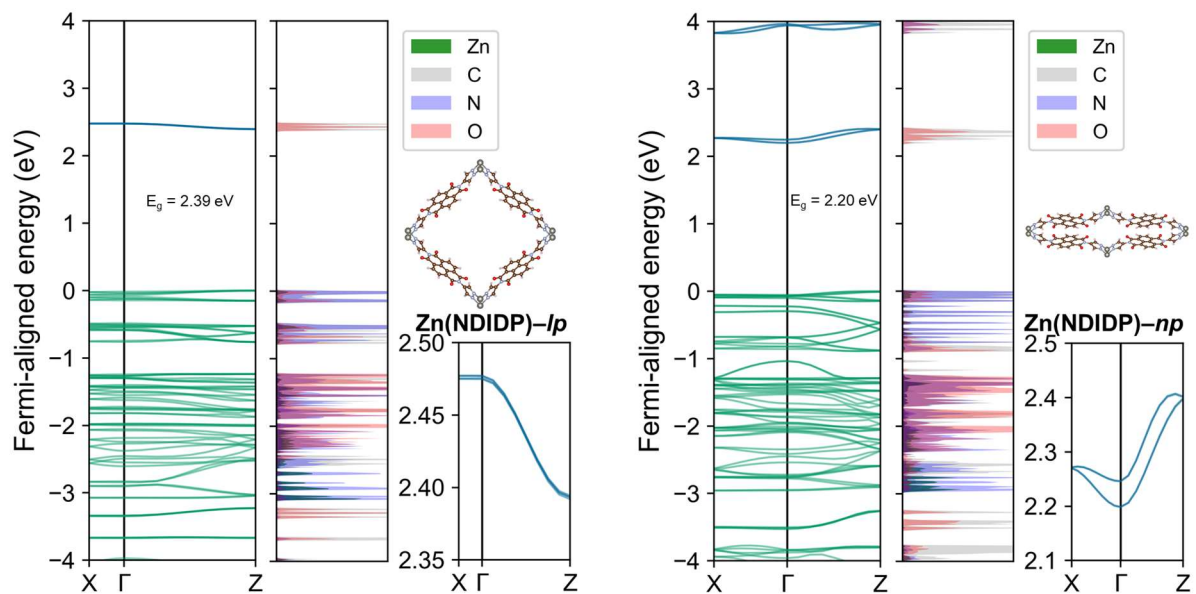
**Figure S8.** Band structure and projected density of states (PDOS) of Zn(NDIDP)–*lp* and Zn(NDIDP)–*np*. Conduction band minima corresponding to NDI are shown separately in the bottom right. Green bands are filled valence bands, and blue bands are empty conduction bands.

**Figure S9.** Band structure and projected density of states (PDOS) of Fe(NDIDP)–*lp* and Fe(NDIDP)–*np*. Conduction band minima corresponding to NDI are shown separately in the bottom right. Green bands are filled valence bands, and blue bands are empty conduction bands. Solid and dotted bands (with lighter color) correspond to up and down spins.
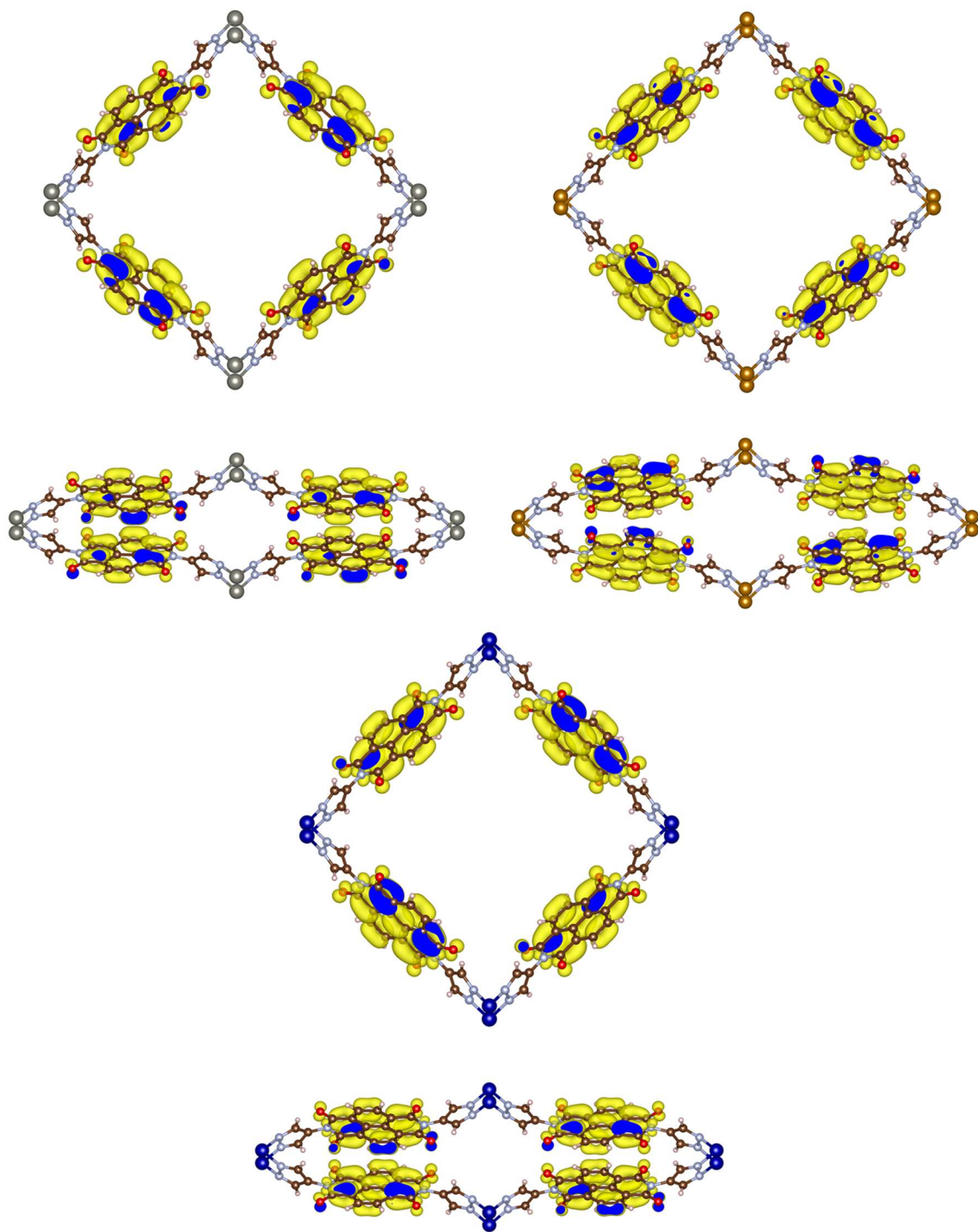
**Figure S10.** Band-decomposed charge density plots of the conduction band minima (CBM) for Zn(NDIDP) (top left), Fe(NDIDP) (top right), and Co(NDIDP) (bottom).
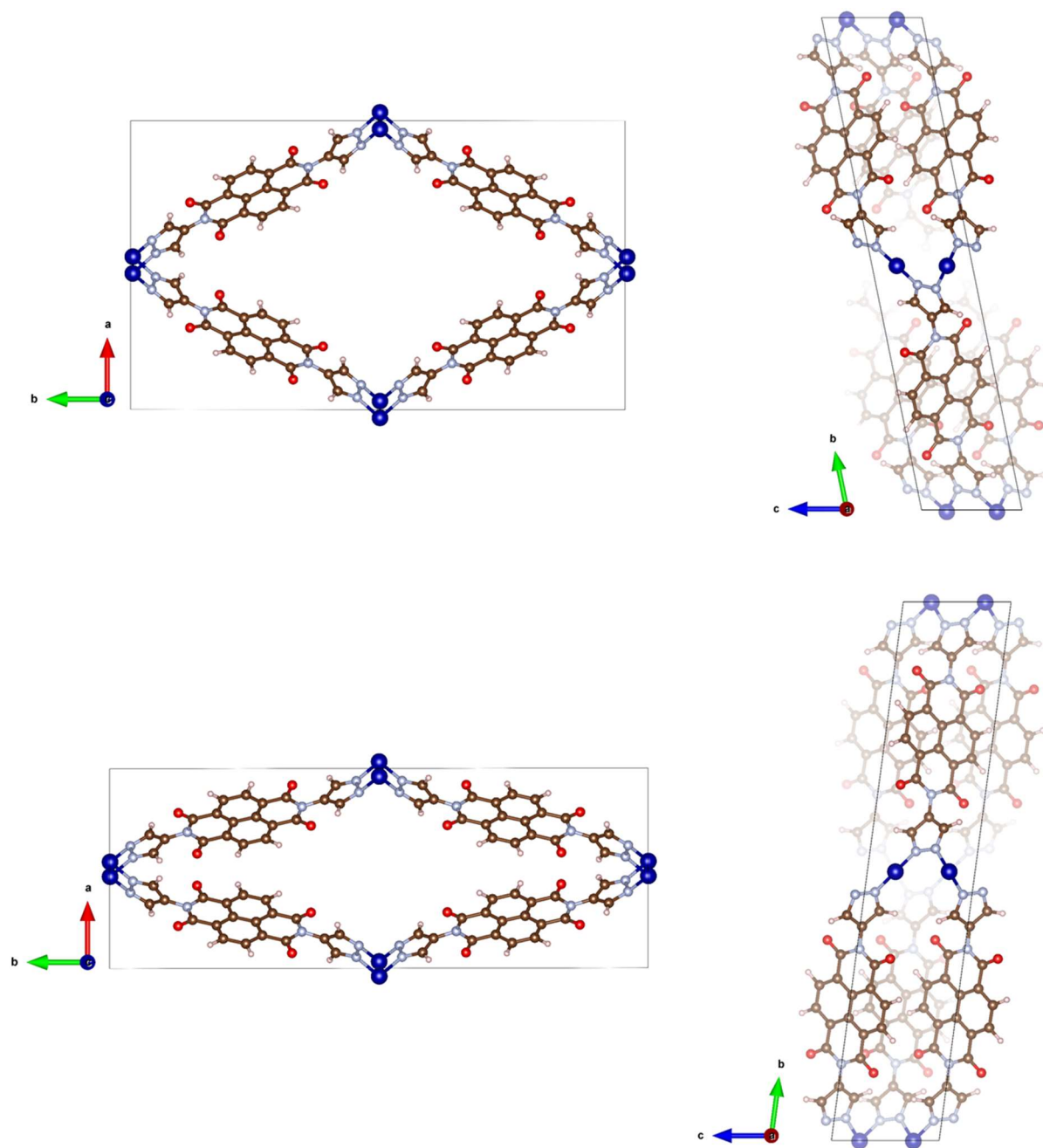
**Figure S11.** Structures of Co(NDIDP) in the *int1* configuration (top) and *int2* configuration (bottom). (blue: Co, brown: C, red: O, light blue: N, white: H)
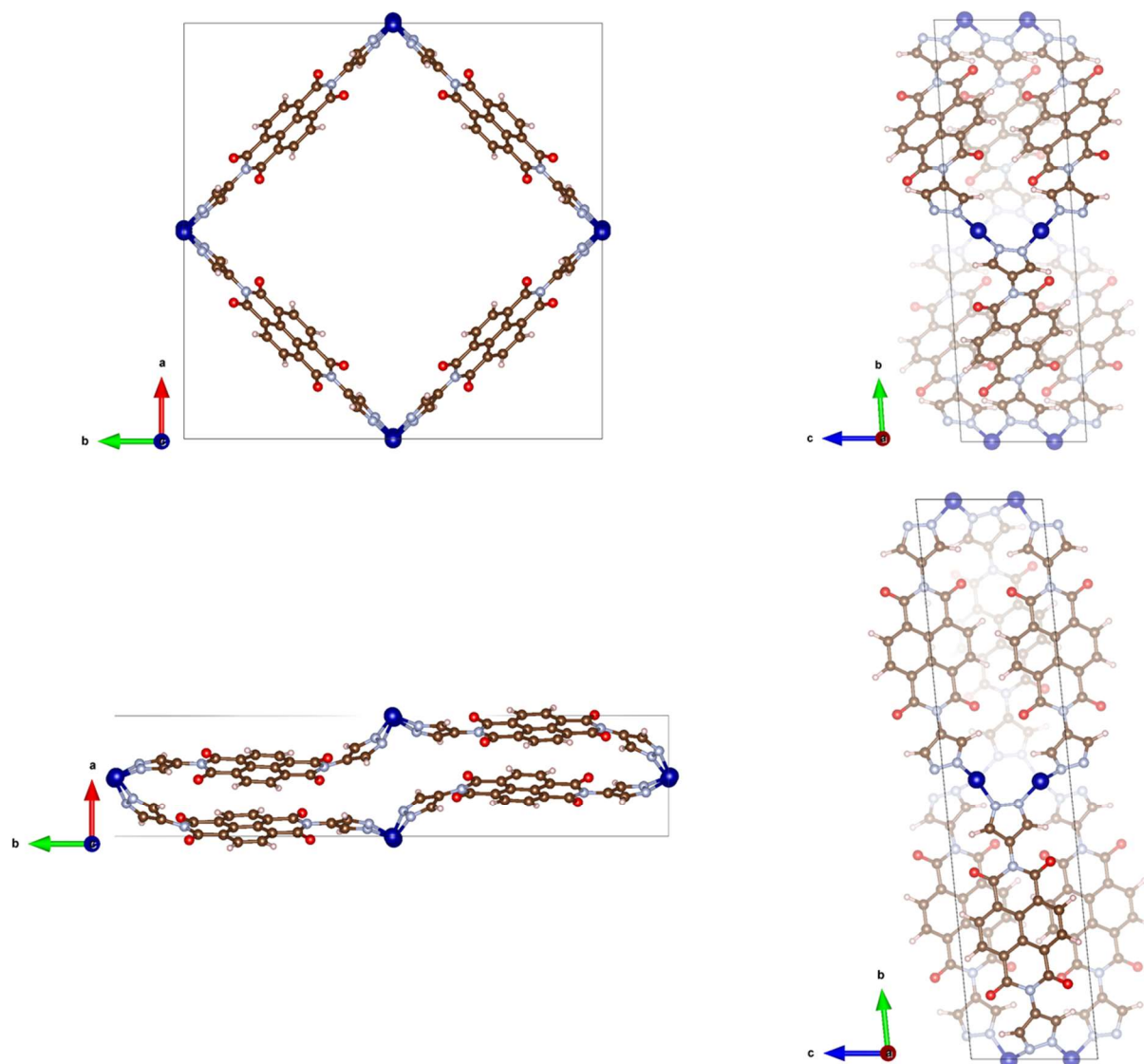
**Figure S12.** Structures of Co(NDIDP) in the *exp* configuration (top) and *sq* configuration (bottom). (blue: Co, brown: C, red: O, light blue: N, white: H)
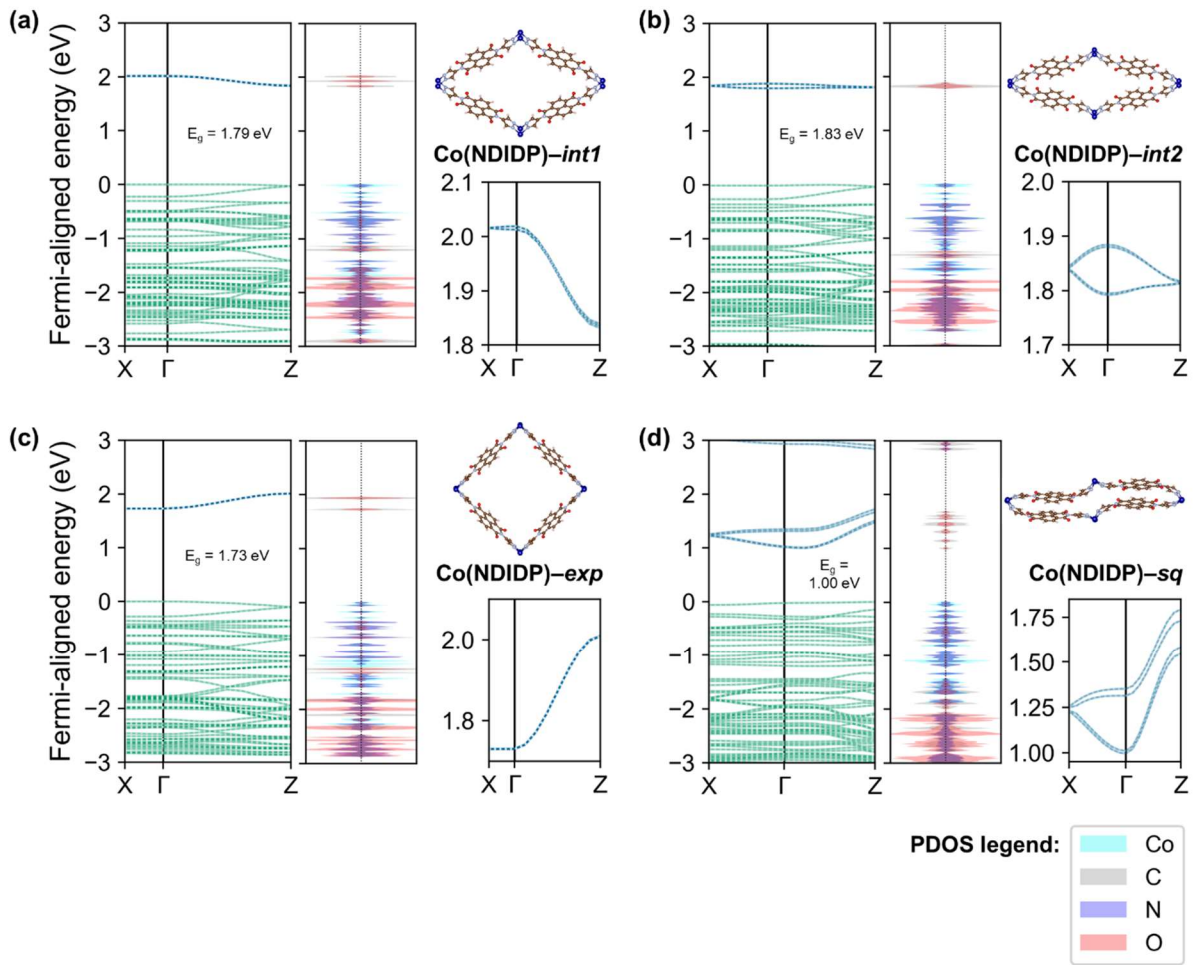
**Figure S13.** Full electronic band structures and projected density of states (PDOS) of Co(NDIDP) in (a) *int1*, (b) *int2*, (c) *exp*, and (d) *sq* configurations. Conduction band minima corresponding to NDI are shown separately in the bottom right. Green bands are filled valence bands, and blue bands are empty conduction bands. Solid and dotted bands (with lighter color) correspond to up and down spins.
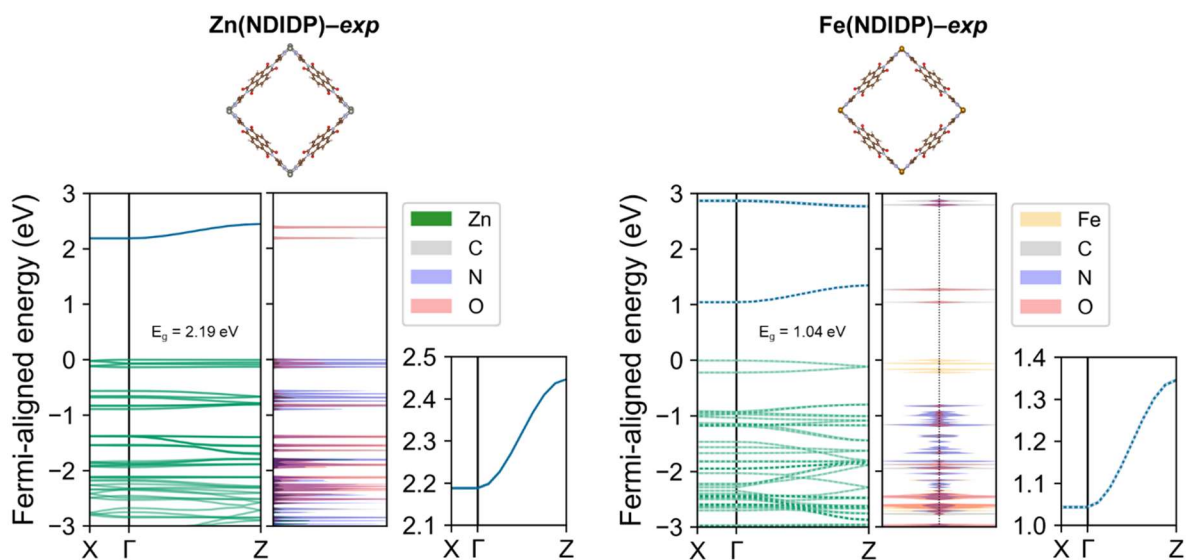
**Figure S14.** Band structures of Zn(NDIDP)–*exp* and Fe(NDIDP)–*exp*. Conduction band minima corresponding to NDI are shown separately in the bottom right. Green bands are filled valence bands, and 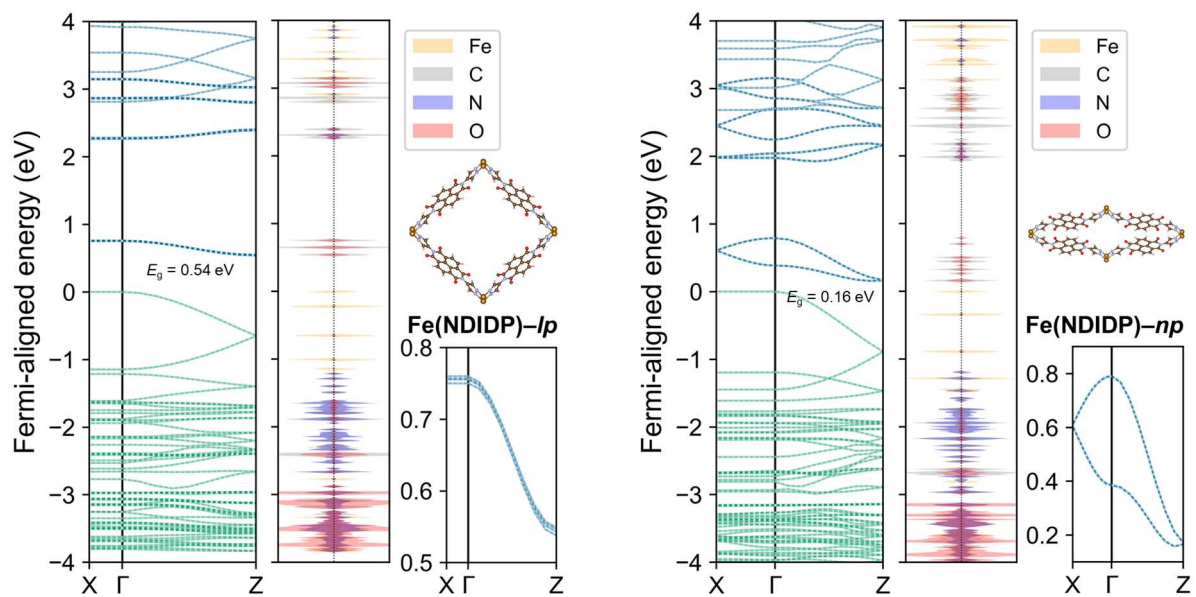blue bands are empty conduction bands. In the case of Fe(NDIDP), solid and dotted bands (with lighter color) correspond to up and down spins.
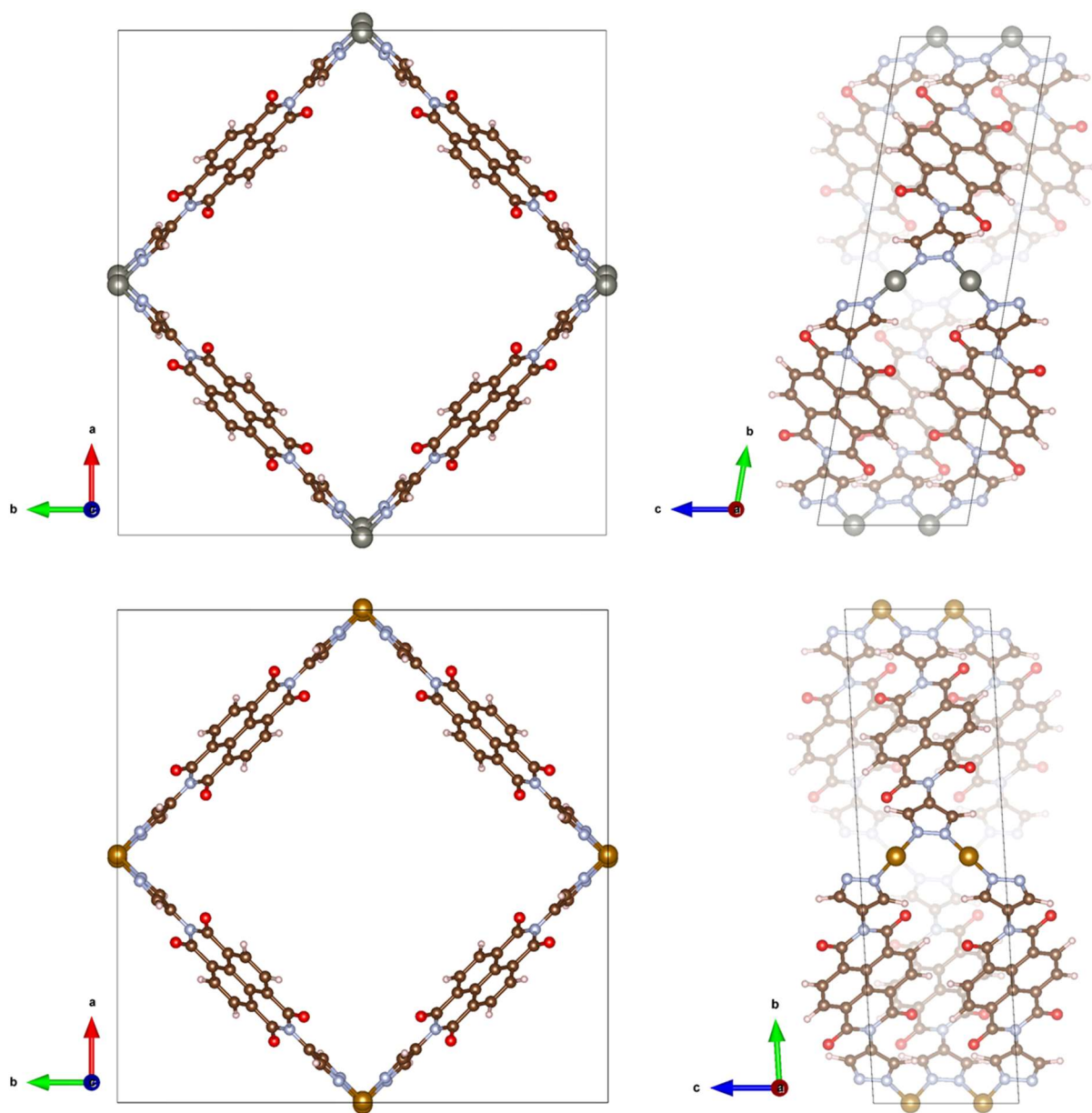
**Figure S15.** Structures of Zn(NDIDP)–*exp* (top) and Fe(NDIDP)–*exp* (bottom). (gray: Zn, gold: Fe, brown: C, red: O, light blue: N, white: H)
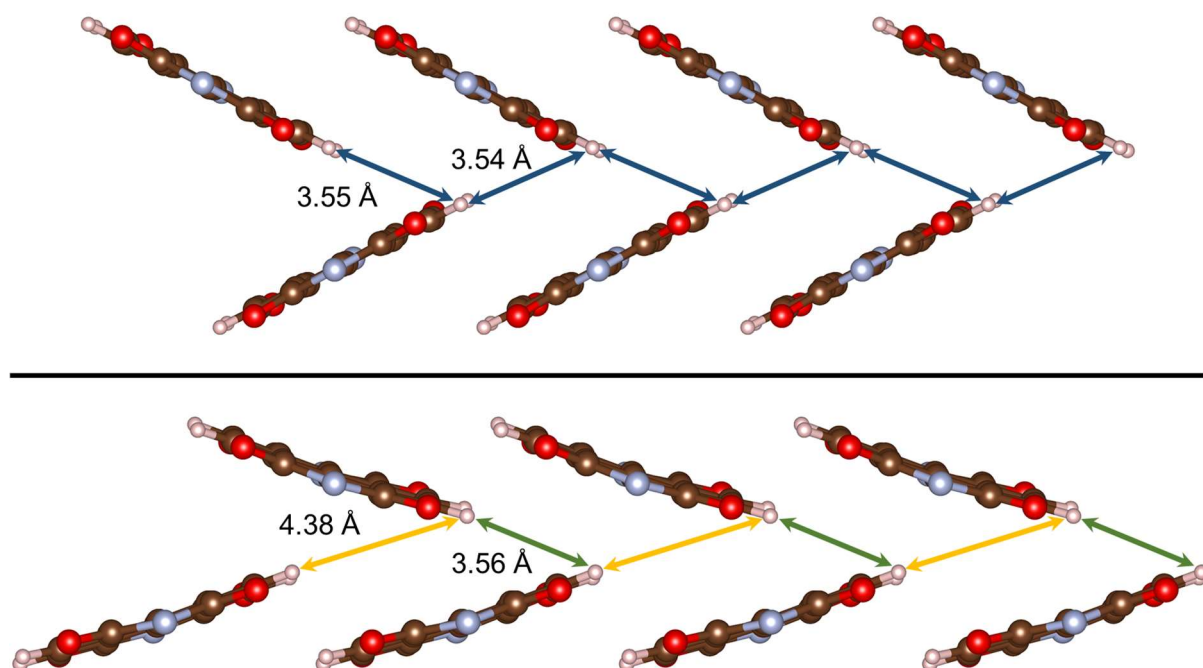
**Figure S16.** Arrangement of NDI moieties stacked along the z-axial direction. Top shows the case of Co(NDIDP)–*np*, and bottom shows Co(NDIDP)–*sq*. H-H distances are displayed to highlight the uneven NDI stacking configuration of Co(NDIDP)–*sq*.
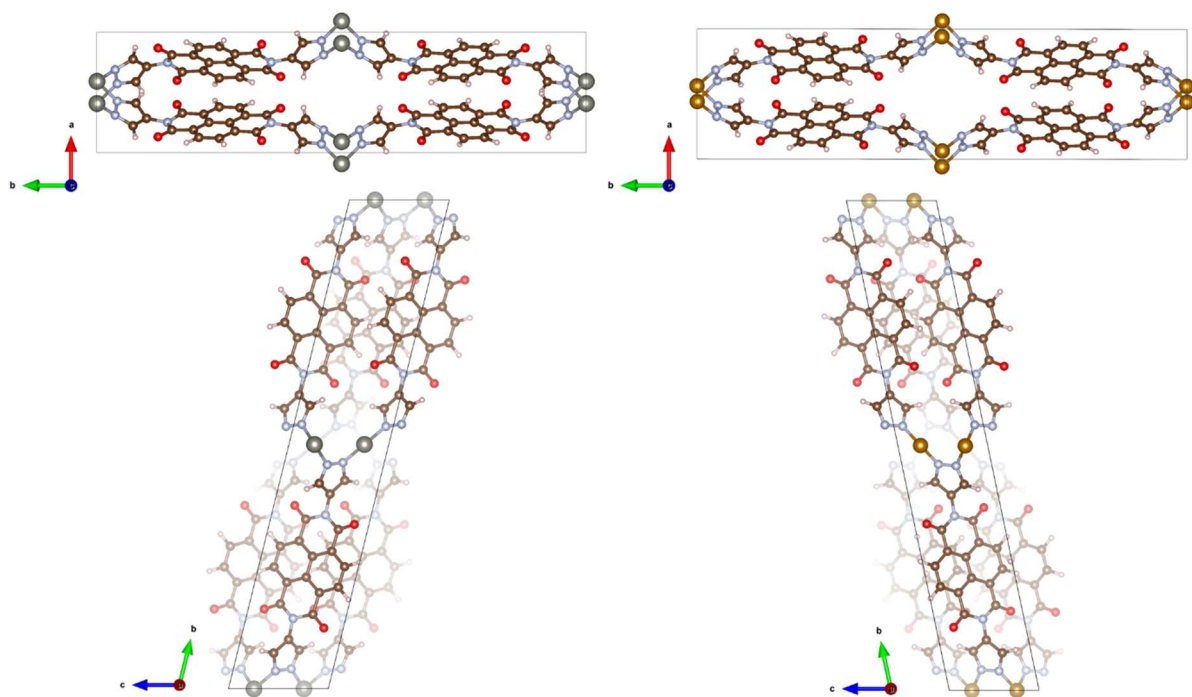
**Figure S17.** Structures of Zn(NDIDP)–*sq* (top) and Fe(NDIDP)–*sq* (bottom). (gray: Zn, gold: Fe, brown: C, red: O, light blue: N, white: H)
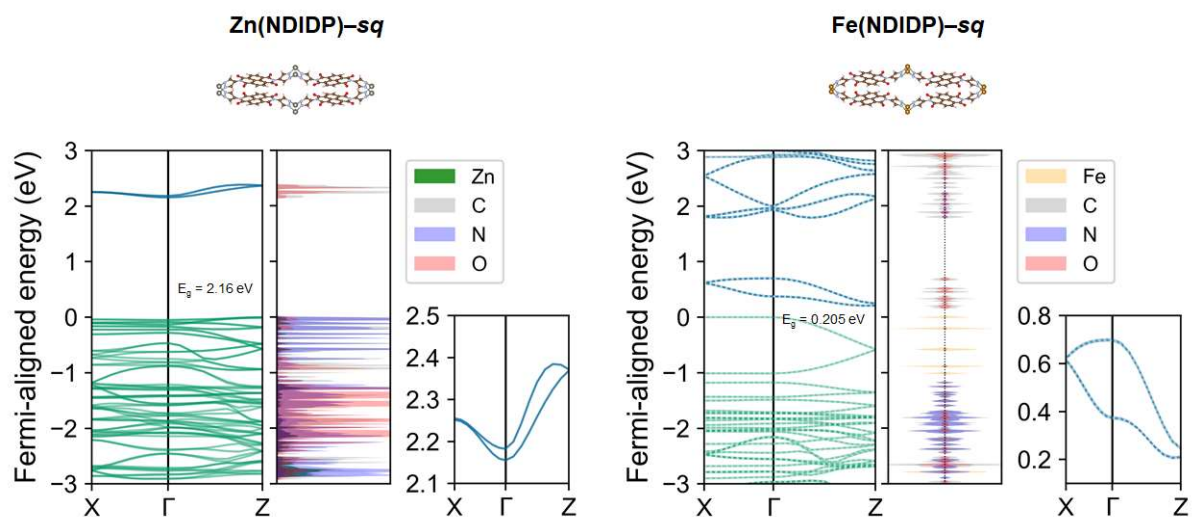
**Figure S18.** Band structures of Zn(NDIDP)–*sq* and Fe(NDIDP)–*sq*. Conduction band minima corresponding to NDI are shown separately in the bottom right. Green bands are filled valence bands, and blue bands are empty conduction bands. In the case of Fe(NDIDP), solid and dotted bands (with lighter color) correspond to up and down spins.
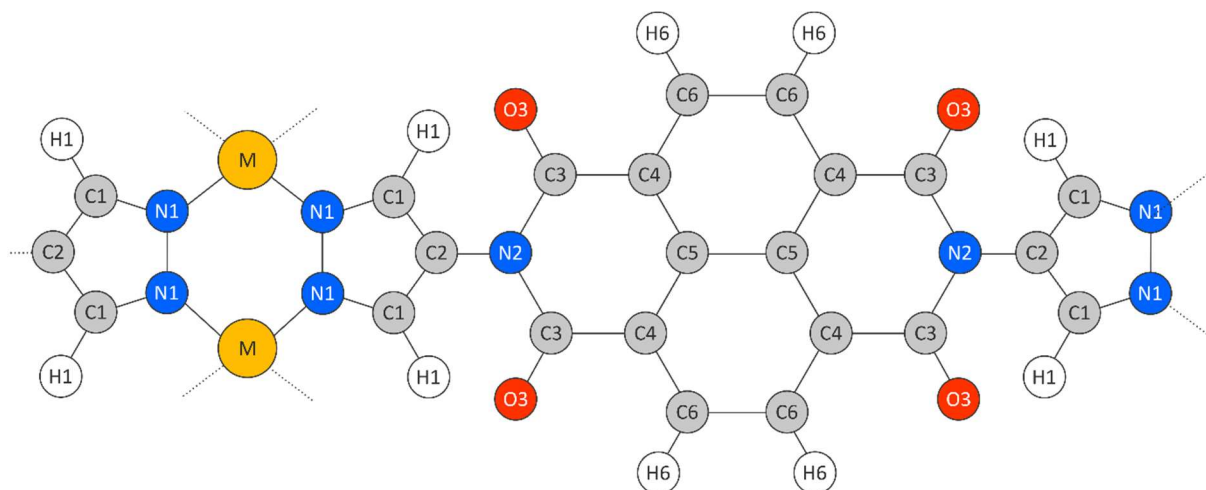
**Figure S19.** Atom types used in the derivation of the three force fields, with M = Zn, Co, or Fe.
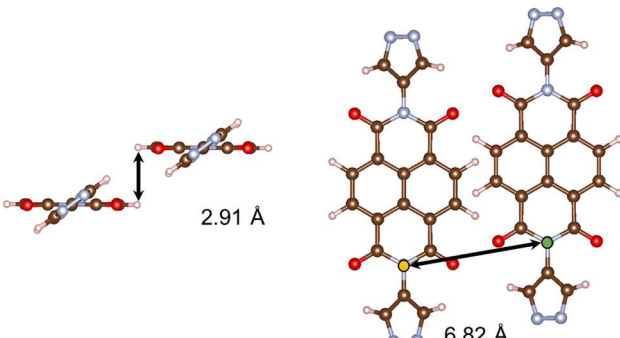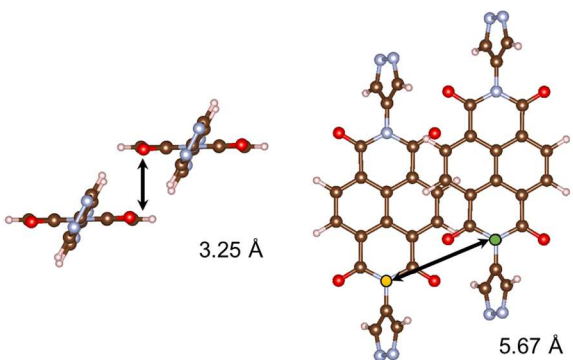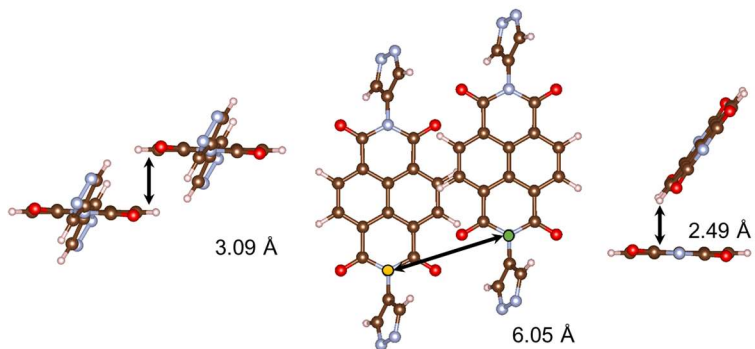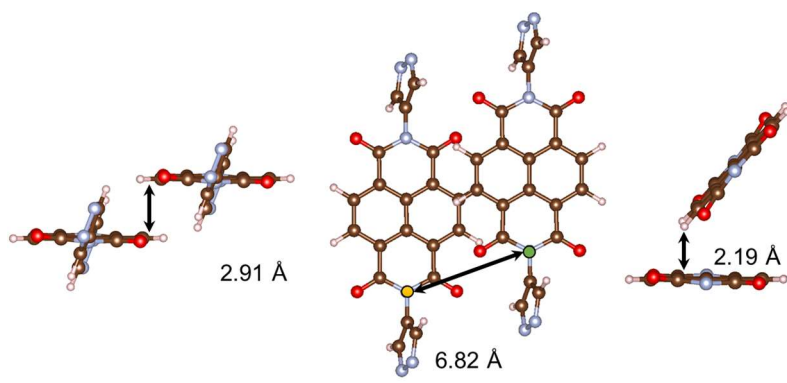
**Table S1.** Lattice parameters of M(NDIDP) (M = Zn, Co, Fe) in various structural configurations considered in this work.

| M(NDIDP) | | a (Å) | b (Å) | c (Å) | α (°) | β (°) | γ (°) | V(Å³) |
|---|---|---|---|---|---|---|---|---|
| Zn | *exp* | 24.96 | 24.55 | 7.45 | 99.66 | 89.99 | 90 | 4499.6 |
| | *lp* | 23.17 | 26.24 | 6.57 | 110.71 | 89.98 | 90 | 3735.4 |
| | *np* | 8.52 | 32.9 | 6.79 | 101.05 | 90.01 | 90 | 1867.6 |
| | *sq* | 7.84 | 32.83 | 6.52 | 103.93 | 89.99 | 90 | 1628.7 |
| Co | *exp* | 24.6 | 24.83 | 7.36 | 86.33 | 89.99 | 90 | 4485.8 |
| | *lp* | 24.14 | 25.34 | 6.36 | 71.56 | 90.03 | 90 | 3688.9 |
| | *int1* | 17.38 | 30.33 | 6.06 | 78.51 | 90.1 | 90 | 3132.2 |
| | *int2* | 11.91 | 32.43 | 6.44 | 97.62 | 90.42 | 90.04 | 2464.9 |
| | *np* | 8.74 | 32.8 | 6.64 | 100.09 | 90.02 | 90.01 | 1875.2 |
| | *sq* | 6.99 | 32.04 | 7.2 | 84.33 | 89.96 | 90.02 | 1604.7 |
| Fe | *exp* | 24.88 | 24.9 | 7.32 | 86.67 | 90.01 | 90 | 4526.7 |
| | *lp* | 23.98 | 26.09 | 6.07 | 75.04 | 89.97 | 90 | 3667.4 |
| | *np* | 10.32 | 33.02 | 5.68 | 80.44 | 90.02 | 89.97 | 1908.3 |
| | *sq* | 8.55 | 32.99 | 5.92 | 78.14 | 90.13 | 89.96 | 1633.8 |
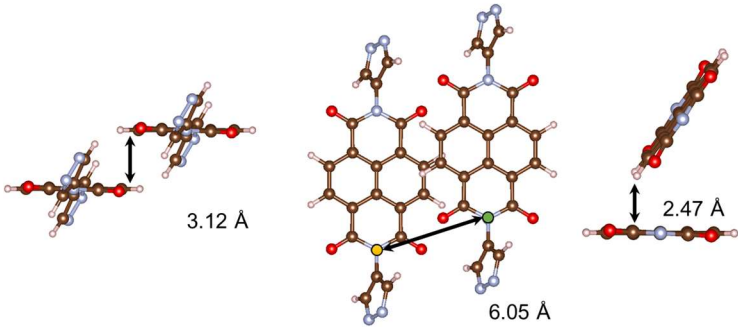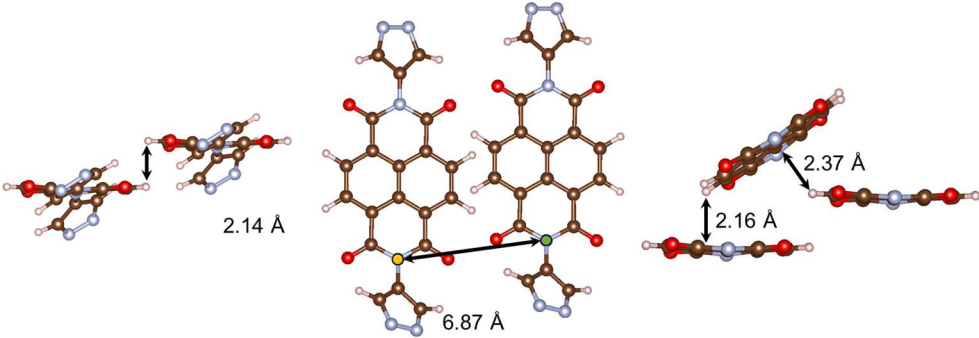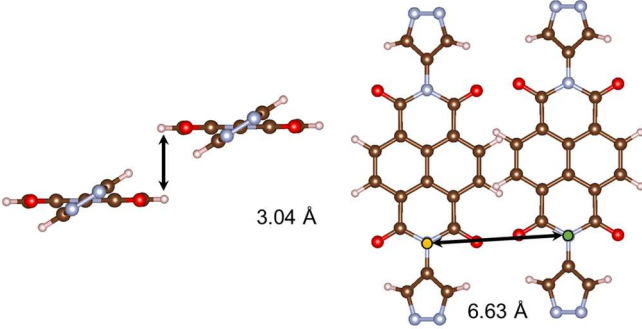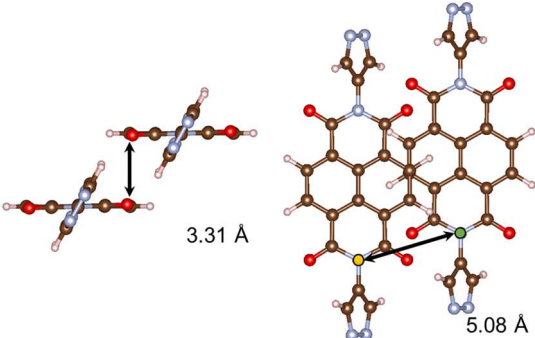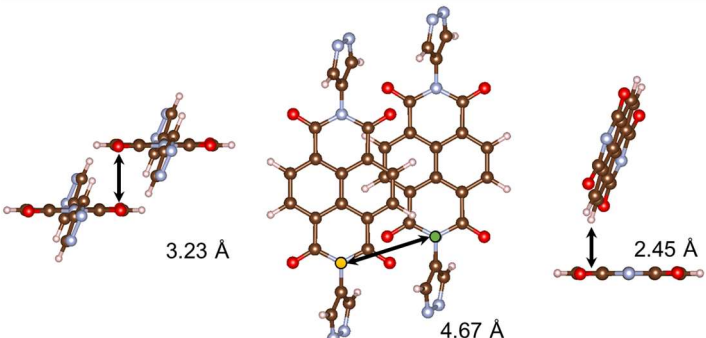
**Table S2.** Average DFT-calculated bond order between the metal ion and pyrazolate N atom in M(NDIDP) (M = Zn, Co, Fe) MOFs. Bond order was calculated using the DDEC6 method developed by T. A. Manz.[S1]

| M(NDIDP) | DFT-calculated M−N bond order | | |
|:---:|:---:|:---:|:---:|
| | *lp* | *np* | difference |
| **Zn** | 2.270 | 2.233 | 0.036 |
| **Co** | 2.498 | 2.453 | 0.044 |
| **Fe** | 2.447 | 2.345 | **0.102** |

**Table S3.** Internal NDI arrangement exhibited by M(NDIDP) (M = Zn, Co, Fe) in the various configurations considered in this work. Edge-to-face configuration along the x-axis is shown when applicable.

| M(NDIDP) | | Internal NDI arrangement |
|---|---|---|
| Zn | *exp* |  |
| | *lp* |  |
| | *np* |  |
| | *sq* |  |

| | | | |
|---|---|---|---|
| Co | *exp* | 3.12 Å<br>6.63 Å | |
| | *lp* | 3.26 Å<br>5.44 Å | |
| | *int1* | 3.40 Å<br>5.01 Å | 4.49 Å |
| | *int2* | 3.61 Å<br>5.29 Å | 3.21 Å |

S23

| Co | np | 3.12 Å  6.05 Å  2.47 Å |
| | sq | 2.14 Å  6.87 Å  2.37 Å  2.16 Å |
| Fe | exp | 3.04 Å  6.63 Å |
| | lp | 3.31 Å  5.08 Å |
| | np | 3.23 Å  4.67 Å  2.45 Å |

| Fe | *sq* |  |



2.89 Å

5.12 Å

2.00 Å
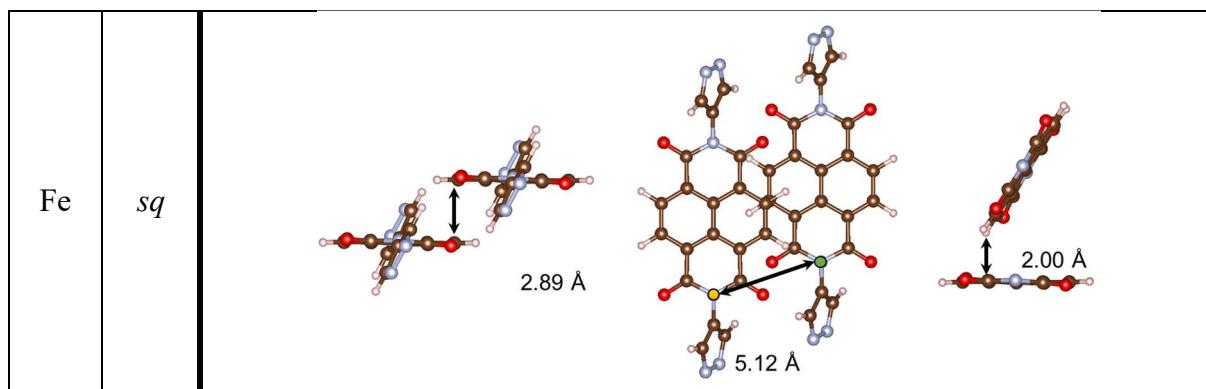
### Flexibility and Conductivity of Zn(NDIDP)-CH₃

To the best of our knowledge, framework flexibility of the zinc pyrazolate MOF with methylated pyrazolate linkers (herein referred to as Zn(NDIDP)-CH₃) has never been extensively considered, neither experimentally nor computationally, in previous studies. This can be primarily attributed to the presence of methyl groups at the 3 and 5 positions of the pyrazolate moiety, which is expected to significantly hinder the range of motion and differentiates this MOF from other well-known flexible MOFs of the same structural motif. Given the robustness of computational methods used in this study, extensive analysis of Zn(NDIDP)-CH₃ was performed to characterize its mechanical and electronic properties.
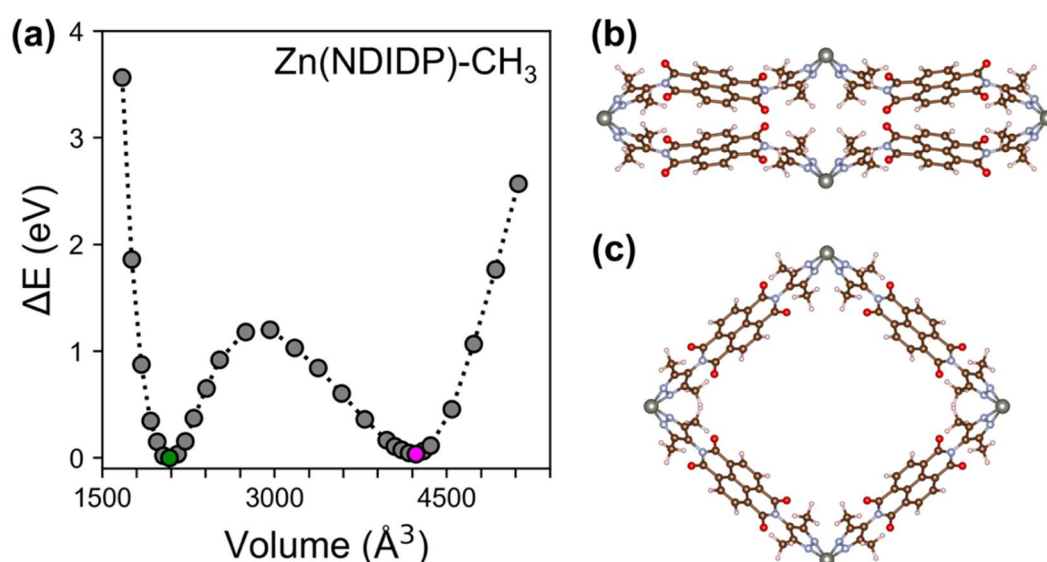


**Figure S20.** (a) $E(V)$ profile of Zn(NDIDP)-CH₃. Green and magenta points correspond to the *np* phase and *lp* phase of the MOFs, and the structures at these volumes are shown in (b) and (c), respectively.

First, the $E(V)$ profile of Zn(NDIDP)-CH₃ was obtained, and is presented in **Figure S20**. Here, energy minimum at $V = 4232.1$ Å³ corresponds to the experimentally observed large pore configuration. Quite interestingly, however, another energy minimum is observed at $V = 2082.6$ Å³, corresponding to a narrow pore configuration that has never been reported experimentally. The global energy minimum is found to be the *np* phase akin to M(NDIDP)s, but the *lp* phase only exhibits a miniscule energy difference of 0.04 eV. Zn(NDIDP)-CH₃ notably exhibits a significantly large energy barrier of 1.20 eV between the *lp* and *np* phases, whereas the energy barrier was 0.12 eV in the case of Zn(NDIDP). This demonstrates that profound differences in the $E(V)$ profile arise from the double methylation of pyrazolate moieties.

Next, the $P(V)$ equation of state of Zn(NDIDP)–CH$_3$ was obtained from MD simulations with DFT-derived force field parameters, and the results are presented in **Figure S21**. From the equation of state, it is revealed that two mechanically stable branches are present. The critical pressure required to force the framework into a potentially present *np* phase is found to be 322 MPa. This pressure is 107 times larger compared to Zn(NDIDP), which in turn proves that double methylation of the pyrazolate moieties in Zn(NDIDP)–CH$_3$ significantly hinders the framework from partaking in the *lp*–to–*np* phase transition. Note that MD simulations at multiple unit cell volumes, shown in pink, were revealed to exhibit a significantly different framework configuration from what was previously predicted from DFT calculations. A sample configuration at $V = 2650$ Å$^3$ is shown in **Figure S22**, which is revealed to have a notably different, overly stacked configuration with the NDI moieties arranged perpendicular to the *z*-axis, and parallel amongst themselves. It was found that all of the other abnormal cases were found to show similar configurations. While these configurations could potentially lead to higher CBM dispersion values, we find further consideration of these new configurations to be beyond the scope of this study. Presence of these secondary phases, especially in the volume range between 2300 and 2750 Å$^3$, leads to an incomplete equation of state for Zn(NDIDP)–CH$_3$. Nonetheless, given the large critical pressure required for the *lp*-to-*np* transition, it can be concluded that double methylation of the pyrazolate moieties significantly hinders the framework flexibility of Zn(NDIDP)–CH$_3$.
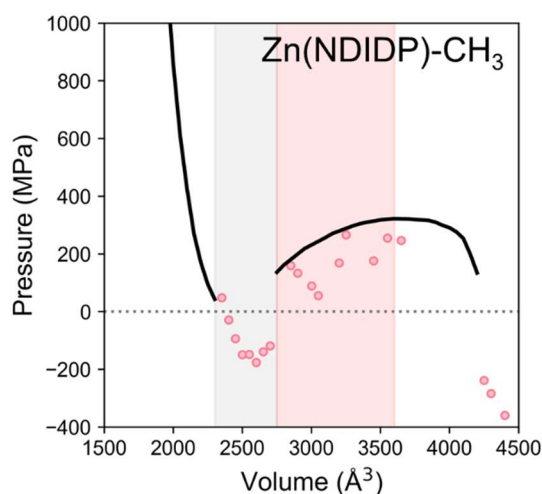


**Figure S21.** $P(V)$ equation of state of Zn(NDIDP)–CH$_3$. Horizontal line at $P = 0.1$ MPa denotes the ambient pressure condition. Pink markers show the data points at which MD simulation deviated away from the main mode of flexibility and exhibited an overly stacked configuration. Regions shaded in red indicate the mechanically unstable volume range as determined by positive $\partial P/\partial V$ values. Mechanical stability is inconclusive in the gray-shaded region due to the lack of points conforming to the main mode of flexibility.
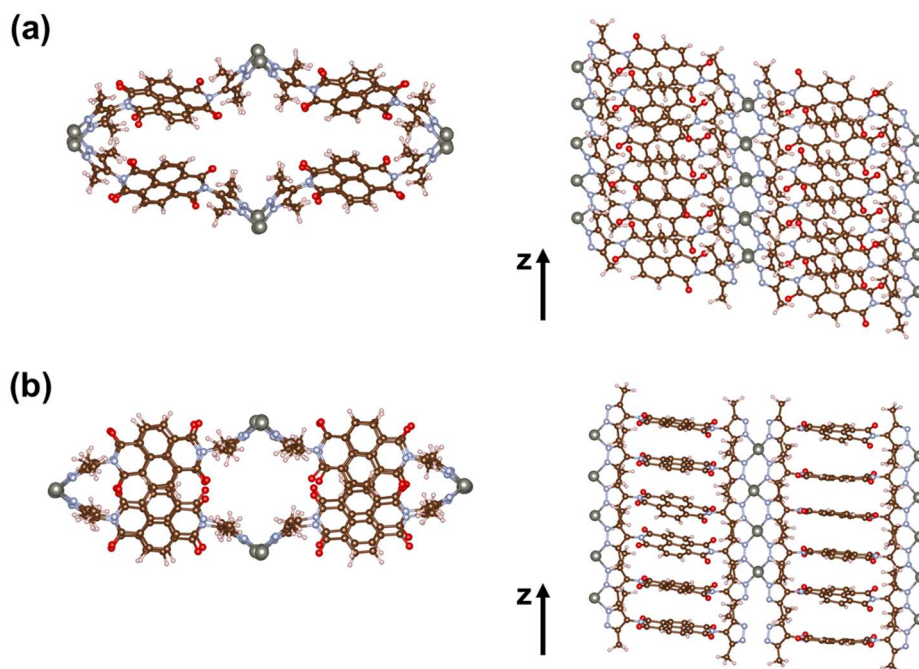
**Figure S22.** Final configurations of Zn(NDIDP)–CH₃ from the MD simulations at unit cell volumes of (a) 2750 Å³ and (b) 2650 Å³. Note that 2750 Å³ follows the main mode of flexibility predicted from the DFT calculations, but the 2650 Å³ deviates away from the expected mode of flexibility and exhibits an overly stacked configuration along the *z*-axis.

Lastly, band structures were computed for the experimentally observed *lp* phase and computationally predicted *np* phase of Zn(NDIDP)-CH₃. Results are presented in **Figure S23**. Consistent with the results presented by Wentz et al., significant conductivity is predicted for Zn(NDIDP)-CH₃-*lp*, given the notable dispersion of CBM with a value of 123 meV in the Γ–Z path ($m_e^* = 4.37m_0$). Differences in the band structures are observed from the previously published results, however, which most likely arise from the differences in DFT methods used for framework optimization and band structure calculations. Zn(NDIDP)-CH₃-*np* shows an increase in the CBM dispersion to 264 meV Γ–Z path, and also the onset of dispersion along the Γ–X path with a value of 45 meV. The band gap also decreases from 2.05 eV to 1.70 eV. Electron effective mass along the Γ–Z path correspondingly decreases from $2.16m_0$ to $0.84m_0$. Relatively smaller dispersion along the Γ–X path results in a larger effective mass of $6.68m_0$. Again, these results are attributed to the rearrangement of NDI moieties as the MOF transitions between the two phases, and the precise internal NDI arrangements are shown in **Figure S24**. Altogether, the results here allow us to conclude that (1) framework flexibility of Zn(NDIDP)–CH₃ is significantly hindered (i.e., larger energy barrier and critical pressure for phase transition) by the presence of methyl groups, as expected, and (2) if the *np* phase can somehow be accessed, improved CT properties could be achieved, akin to the M(NDIDP) MOFs.

**Figure S23.** Electronic band structures and projected density of states (PDOS) of Zn(NDIDP)–CH$_3$ in the (a) *lp* and (b) *np* phases. Conduction band minima corresponding to NDI are shown separately in the bottom right. Green bands are filled valence bands, and blue bands are empty conduction bands.



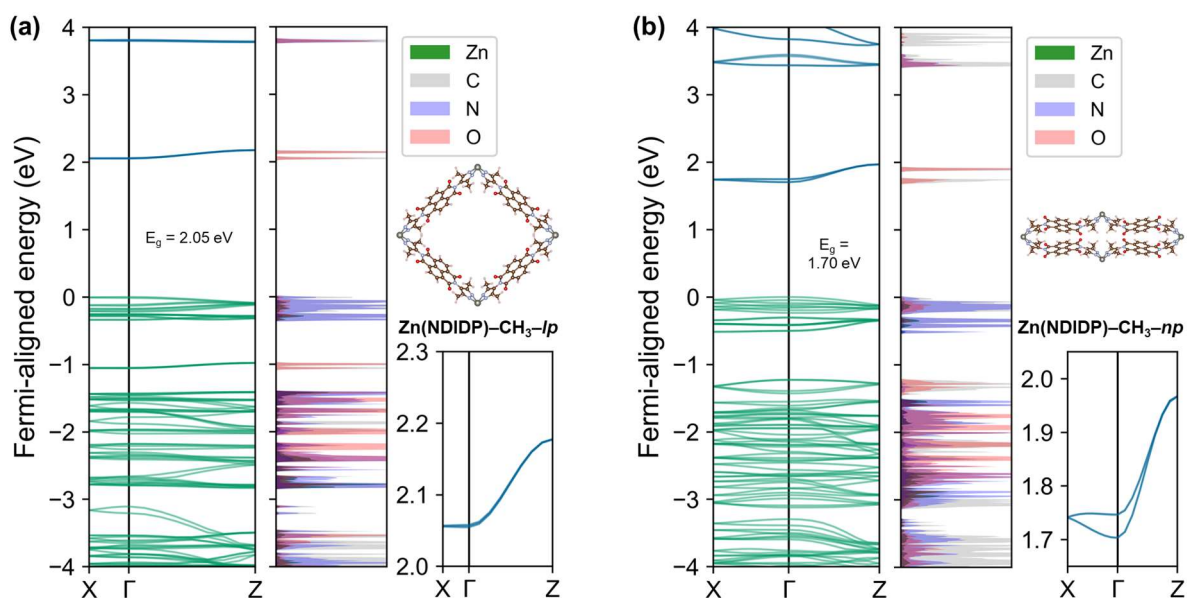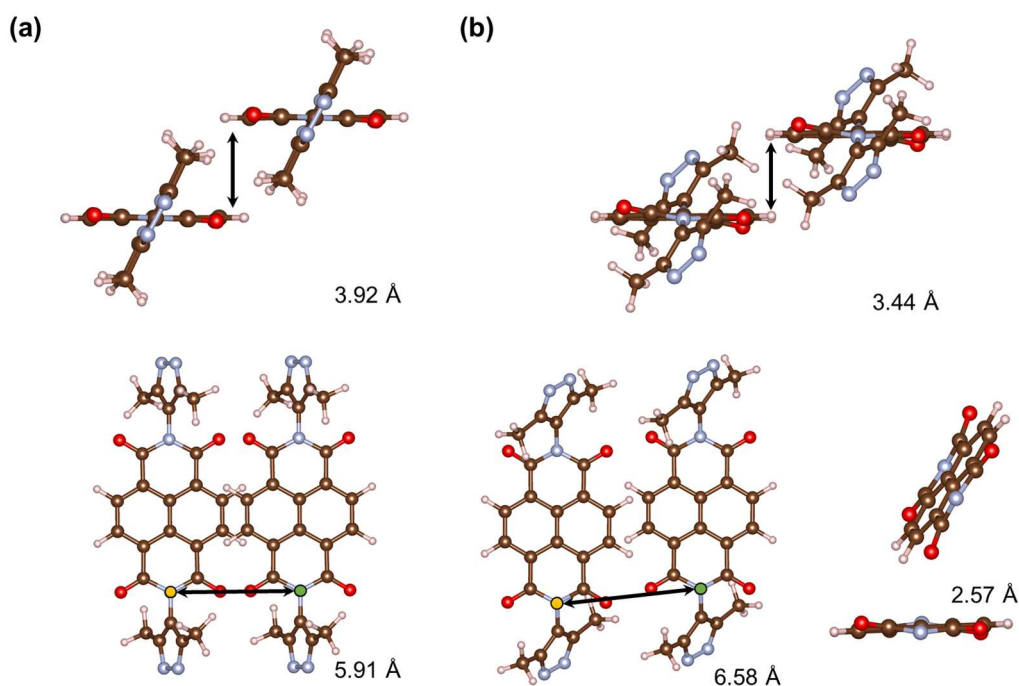**Figure S24.** Internal NDI arrangements exhibited by Zn(NDIDP)–CH$_3$ in the (a) *lp* and (b) *np* phases.

### *Secondary Phase Configurations of Fe(NDIDP)*

In the MD simulations conducted for the derivation of $P(V)$ equations of state, Fe(NDIDP) in the volume range between 3250 and 3800 Å$^3$ was found to exhibit peculiar MD trajectories, where two different clusters of $a$ lattice parameters can be found (**Figure S25**). Upon a closer look, this was revealed to be caused by the existence of a secondary phase to which the MOF can transition under the given simulation conditions. However, this secondary phase, shown in **Figure S7**, shows a larger $a$ lattice parameter than expected, which is almost equivalent to the $b$ lattice parameter and hence results in a square-like configuration when viewed along the z-axial direction. Interestingly, however, the framework is found to have been significantly sheared in the *yz* direction, which takes place because of the volume constraint. Since such a configuration deviates away from the main mode of M(NDIDP) flexibility, where the framework expands or contracts by taking advantage of its wine rack motif, we have labeled these configurations as a secondary phase of the MOF. In the data analysis, we have hence differentiated the data points pertaining to the main phase and secondary phase by tracking the $a$ lattice parameter and plotted them separately. This phenomenon is unique to Fe(NDIDP), and we suspect that this is also caused by the softer binding of Fe, which allows the MOF to overcome the energy barriers associated with the MOF going from the main phase to secondary phase.



**Figure S25.** Pressure vs $a$ lattice parameter scatter plot from the MD simulation conducted for Fe(NDIDP) at $V$ = 3250 Å$^3$. Two distinct clusters are observed, which correspond to the configuration following the main mode of expansion/contraction (lower $a$ parameter), and the significantly sheared configuration (higher $a$ parameter).

### *VBM Dispersion in M(NDIDP)*

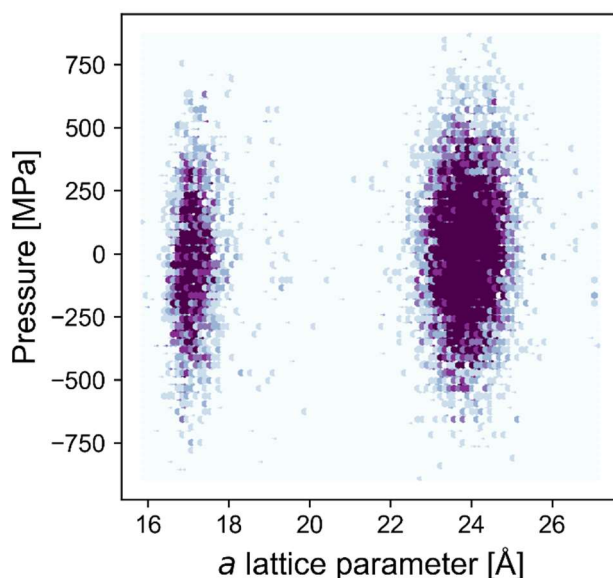In this study, our analysis of conductivity and CT in M(NDIDP) MOFs has primarily revolved around the dispersive CBM found in their band structure, which is solely composed of the orbitals provided by newly installed NDI moieties. Such exclusive focus was safely put on CBM since it undoubtedly pertains to the new CT pathways that have been constructed in the MOFs via modular design. However, it should be noted that large dispersions are also present in the valence band maximum (VBM) in some cases, especially for Fe(NDIDP). Here we explain that these VBM dispersions are most likely artefacts of DFT modeling, and should not be interpreted as indications of efficient hole transport. From the PDOS and band-decomposed charge density plot corresponding to the VBM (**Figure S26**), VBM are revealed to be comprised of Fe only. This would signify that VBM dispersions arise from the direct orbital overlap between Fe ions. However, in reality, such overlaps are highly unlikely as the adjacent metal ions are bridged by two N atoms and exhibit $(-Fe-N-N-)_\infty$ binding pattern. As a matter of fact, Fe-to-Fe distance of 3.13 Å found in our DFT relaxed Fe(NDIDP) structures is abnormally short compared to the experimental distance of 3.6 Å observed in Fe(BDP). This means that interactions between adjacent metal ions are overexaggerated. Hence, we conclude that dispersive VBMs are caused by the falsely heightened spin coupling between the metals, which is a known issue of the DFT methods adopted in this study.[S2–S5] We do note, however, that other 1D Fe−azolate clusters are known to secure the CT pathways in previously known conductive MOFs. Therefore, it could be possible to combine the CT pathways provided by NDI moieties with CT pathways of capable metal clusters, resulting in highly conductive MOFs capable of ambipolar transport.
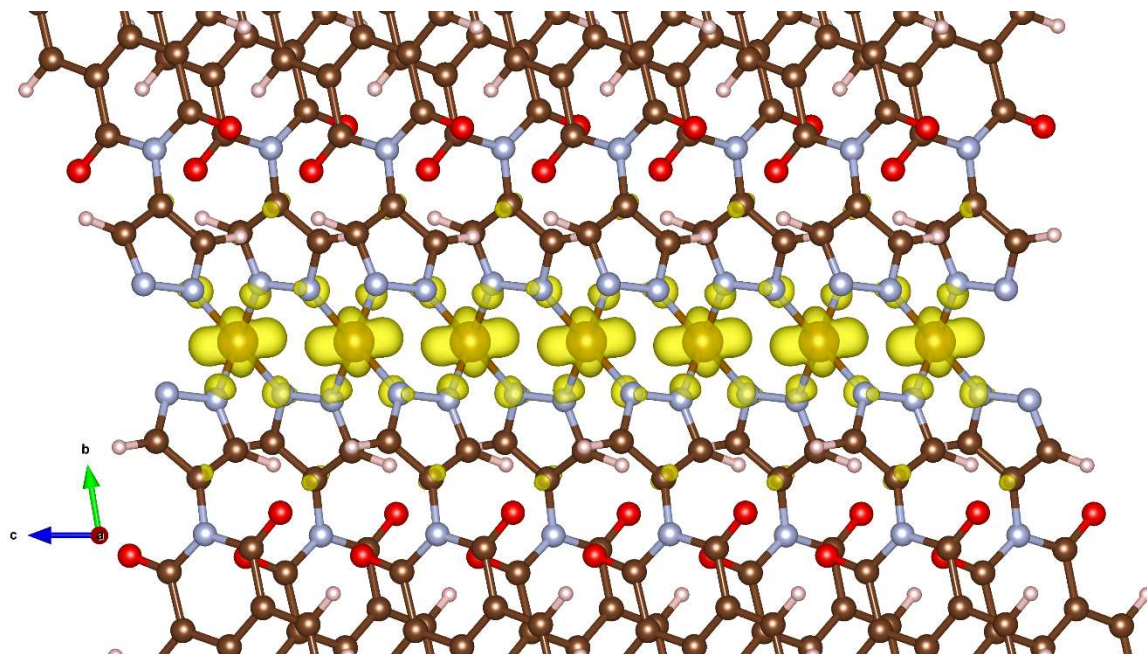
**Figure S26.** Band-decomposed charge density plot of the valence band maximum (VBM) for Fe(NDIDP).

## *CBM Splitting/Folding in Smaller Volume Configurations*

It is important to accurately interpret the band structures that have been obtained for M(NDIDP). Precisely, apparent breakage of energy degeneracy in the CBM at lower volumes of the MOFs must be considered. This is primarily attributed to the presence of multiple electronic units within the unit cell that come closer together with framework contraction. As discussed in the main text, each NDI moiety serves as an electronic unit that could lead to significant band dispersion if they are arranged in a manner that leads to electronic coupling with its own replicas in the adjacent unit cells. Note that four organic linkers are present in the unit cell of M(NDIDP) (**Figures S1-S3**), and two pairs can be identified along the *x*-axial direction. In the larger volume configurations, these NDI pairs exist far enough from each other so that electronic coupling within the unit cell does not occur. Each NDI then only undergoes coupling with its own images along the *z*-axis, and hence four different bands with almost identical shapes are found in the resulting band structures (left of **Figure S27**). In the contracted, smaller volume configurations, the two NDI moieties exist in close enough proximity for significant electronic coupling with one another. Hence, their interactions lead to the breakage of energy degeneracy and the four bands are now arranged in two lower energy bands corresponding to the bonding interactions and two higher energy bands corresponding to the antibonding interactions. As shown in the right of **Figure S27**, relative arrangement of the NDI moieties leads to the presence of multiple electronic units along both the *x*- and *z*-axes. As a result, bands pertaining to NDI, such as the CBM, can be interpreted as having been "folded" due to the presence of multiple electronic units interacting with one another in the unit cell.
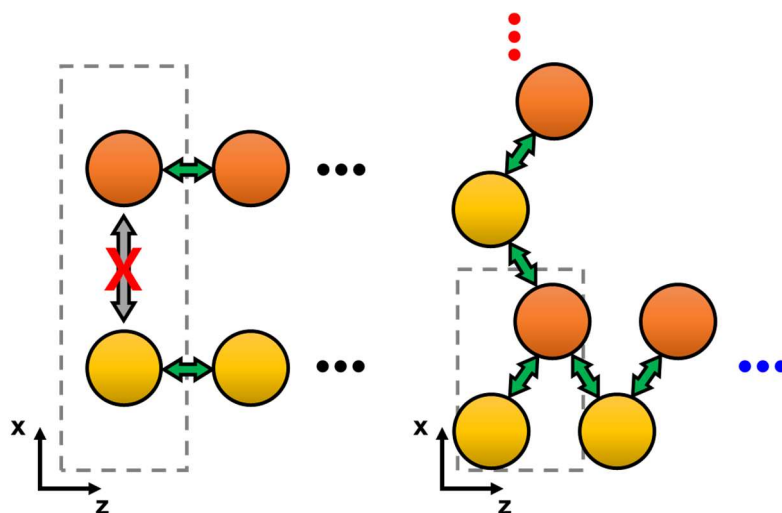


**Figure S27.** Schematics showing the arrangement of NDI moieties in the unit cell in larger volume and smaller volume configurations.

### *Calculations at the DFT+U Theory-Level*

In this study, a hybrid functional method (i.e. HSE06) was employed in the band structure calculations to effectively account for the self-interaction error of conventional DFT approaches in describing the electronic structures of the MOFs. For computational efficiency, however, geometry optimization for the acquisition of various MOF configurations at different volume points were performed at the non-hybrid functional theory level (i.e. PBE-D3(BJ)). However, it should be noted that the self-interaction error could also affect the geometry optimization results of MOFs. As such, additional calculations were conducted to account for the effects of self-interaction error on the precise geometries of the M(NDIDP) MOFs under different framework configurations. MOF geometry optimization for a range of unit cell volumes were repeated at the PBE+U-D3(BJ) theory level, where the U correction approach is used to empirically account for the self-interaction error of the transition metal d electrons. Here, it is importantly noted that the accuracy of U correction method is highly dependent on the appropriate choice of U correction parameters. However, validated system-specific parameters for the M(NDIDP) MOFs are non-existent. Hence, $U_{eff}$ correction parameters of 7.5, 3.3, and 4.0 eV for Zn, Co, and Fe found in the literature for relevant material systems were used.[S6-S7]
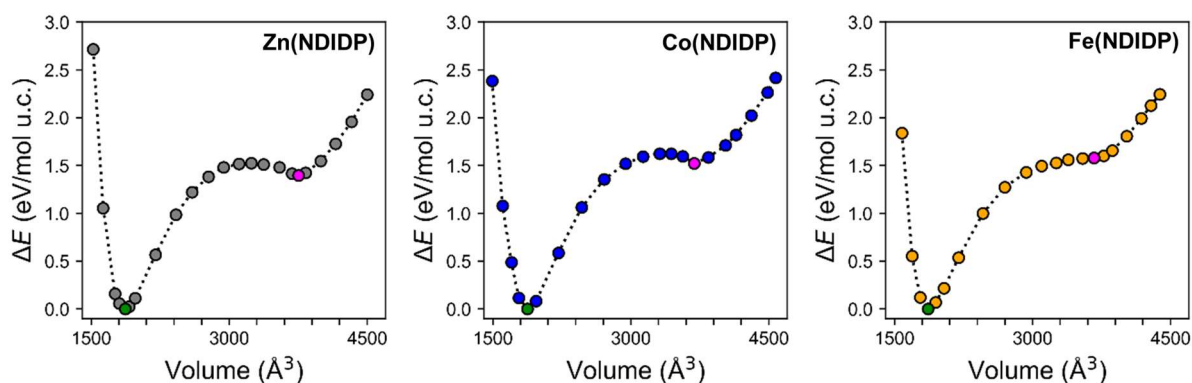


**Figure S28.** *E* vs *V* profiles of Zn(NDIDP) (top left), Co(NDIDP) (top right), and Fe(NDIDP) (bottom) calculated at the DFT+U-D3(BJ) theory level. Note that in each profile, the green data point corresponds to the global minimum *np* phase, and the pink data point corresponds to the metastable (or unstable for Fe(NDIDP)) *lp* phase of the MOF.

**Figure S28** shows the resulting *E* vs *V* profiles of the three M(NDIDP) MOFs at the PBE+U-D3(BJ) theory level. When compared with the original results presented in **Figure 2**, no significant changes in the overall trends are found. That is, both Zn(NDIDP) and Co(NDIDP) exhibit a global minimum corresponding to the *np* phase, and a local minimum in the higher

volume range that corresponds to the *lp* phase. In the case of Fe(NDIDP), only a single global minimum is found for the *np* phase, and a local minimum for the *lp* phase continues to be absent. It is interestingly noted that the shoulder-like feature or the "plateauing" effect observed in Fe(NDIDP) has become relatively more prominent in the newly performed calculations at the PBE+U-D3(BJ) theory level. Such changes can be attributed to the localized description of Fe d electrons via the U correction approach.

For the *lp* and *np* phases of M(NDIDP) MOFs, band structures and projected density of states (PDOS) were additionally calculated at the PBE+U-D3(BJ) theory level. Results are presented in **Figures S29-S31** and **Table S4**. In all of the MOFs, conduction band minimum (CBM) is consistently observed to be solely comprised of the C and O atoms, which can be attributed to the NDI moieties. As such, for these MOFs at the new theory level, it equally suffices to focus on the CBM of the MOF system in analyzing their CT properties. Significantly, it is observed in all three M(NDIDP) MOFs that the shift from 1D to 2D CT takes place as the MOF transitions from the *lp* phase to *np* phase (see **Table S4**). This importantly confirms that even under the new level of theory, the transition from 1D to 2D CT consistently takes place.

Note that there exists a significant diminishment in the CBM dispersion for Fe(NDIDP)-*np* when compared with the previous results in **Figure S9**. This arises from the notably less overlap between NDI moieties (see **Figure S32**), as evident from the increased planar alignment offset from 4.67 to 5.79 Å. Significant diminishment of the band dispersion to a near-zero value is also interestingly observed for Zn(NDIDP)-*lp*, although the NDI arrangements are found to be quite similar to the previously obtained configuration (see **Figure S33**). In this case, it is conjectured that NDI moieties are arranged in such a manner where the bonding and antibonding interactions between the positive and negative phases of $\pi^*$ NDI molecular orbitals are balanced out. Such non-conducting behavior in the *lp* phase of the MOF is desirable, as the MOF would then be able to transition from near-zero transport to significant transport in two dimensions, constituting an on-and-off behavior.
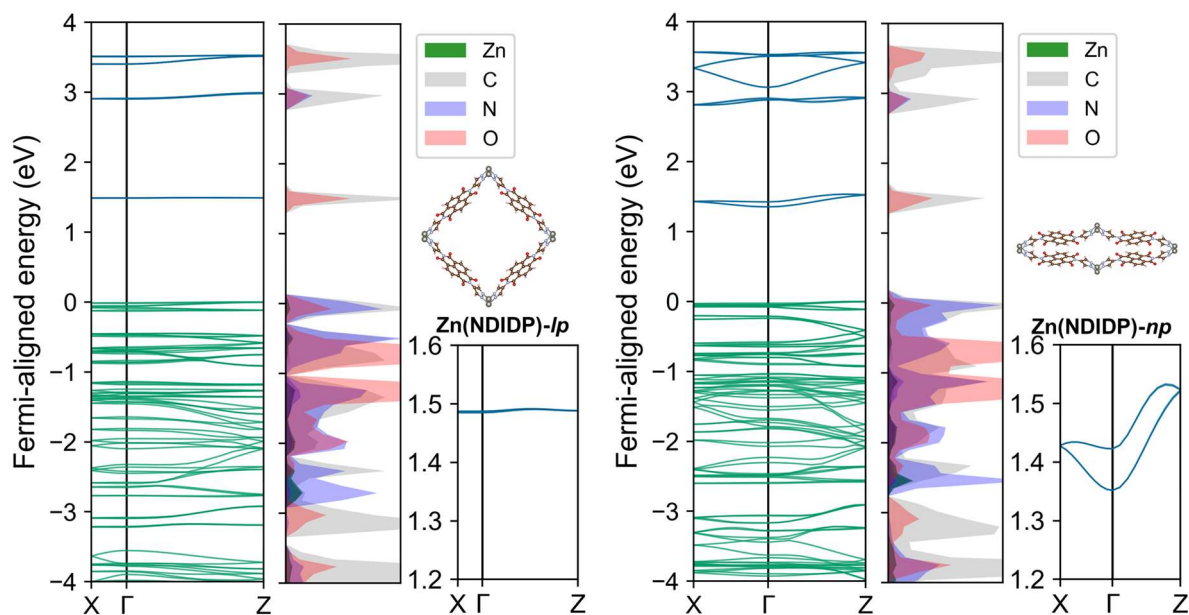
**Figure S29.** Electronic band structures and projected density of states (PDOS) of Zn(NDIDP)–*lp* (left) and Zn(NDIDP)–*np* (right). Conduction band minima corresponding to NDI are shown separately in the bottom right. Green bands are filled valence bands, and blue bands are empty conduction bands.



**Figure S30.** Electronic band structures and projected density of states (PDOS) of Co(NDIDP)–*lp* (left) and Co(NDIDP)–*np* (right). Conduction band minima corresponding to NDI are shown separately in the bottom right. Green bands are filled valence bands, and blue bands are empty conduction bands. Solid darker lines and lighter dotted lines correspond to up and down spins, respectively.

**Figure S31.** Electronic band structures and projected density of states (PDOS) of Fe(NDIDP)–*lp* (left) and Fe(NDIDP)–*np* (right). Conduction band minima corresponding to NDI are shown separately in the bottom right. Green bands are filled valence bands, a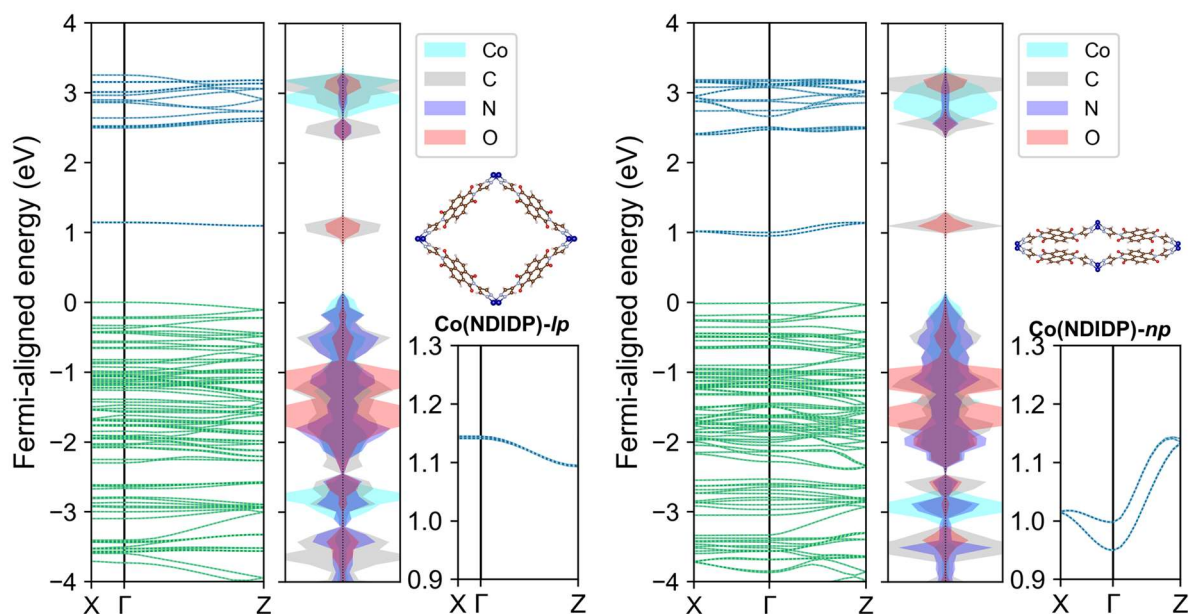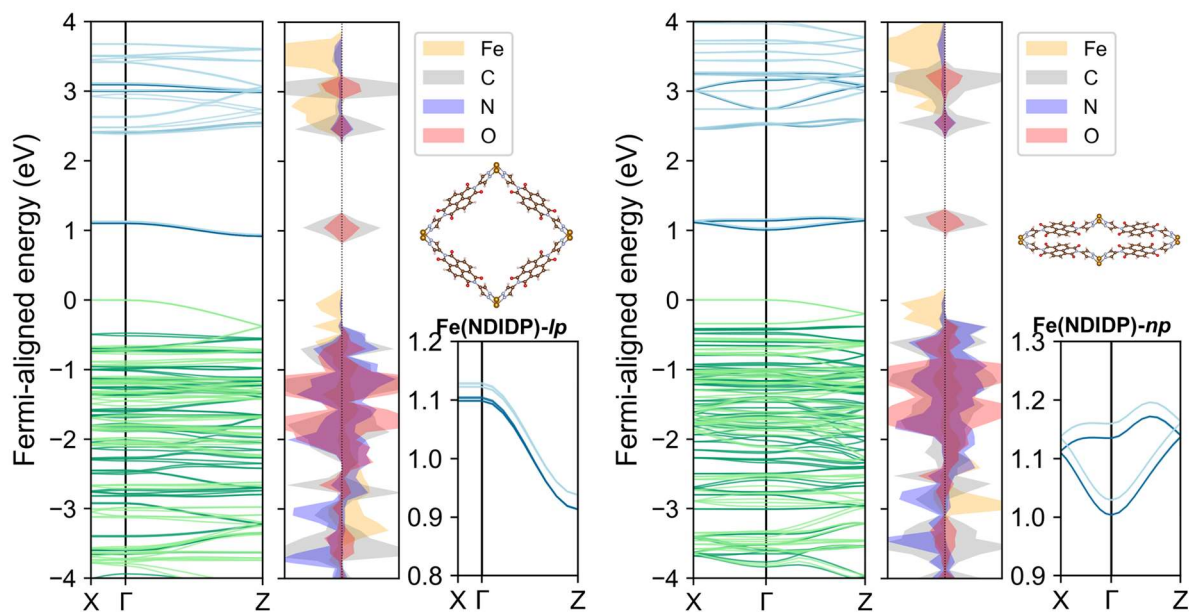nd blue bands are empty conduction bands. Darker colored lines and lighter colored lines correspond to up and down spins, respectively.

**Table S4.** CBM dispersion values and corresponding effective masses of electron ($m_e^*$) obtained from the band structures of M(NDIDP)–*lp* and M(NDIDP)–*np*, with MOF configurations obtained at the PBE+U-D3(BJ) theory level. ($m_0$: electron rest mass)

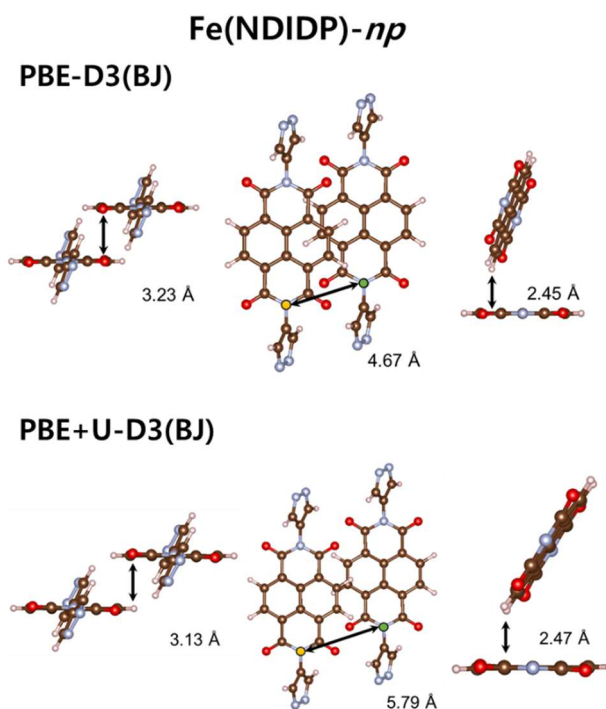| M(NDIDP) | large pore (*lp*) | | narrow pore (*np*) | |
|---|---|---|---|---|
| | Γ–X | Γ–Z | Γ–X | Γ–Z |
| Zn | | 5 meV $m_e^* \rightarrow \infty$ | 87 meV $m_e^* = 3.09m_0$ | 179 meV $m_e^* = 1.93m_0$ |
| Co | 0 meV $m_e^* \rightarrow \infty$ | 51 meV $m_e^* = 7.05m_0$ | 66 meV $m_e^* = 3.39m_0$ | 188 meV $m_e^* = 1.71m_0$ |
| Fe | | 190 meV $m_e^* = 2.18m_0$ | 128 meV $m_e^* = 2.42m_0$ | 165 meV $m_e^* = 2.53m_0$ |

**Figure S32.** Arrangement of NDI moieties in Fe(NDIDP)-*np* obtained at different theory levels. Left and middle figure show the arrangement of NDI along the *z*-direction. Right figure shows the closest contact between adjacent NDI moieties along the *x*-direction.
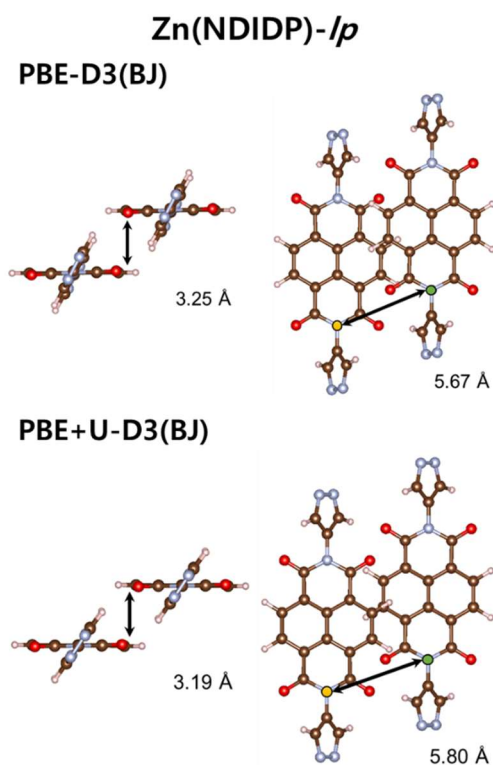


**Figure S33.** Arrangement of NDI moieties in Zn(NDIDP)-*lp* obtained at different theory levels. Both figures correspond to the arrangement of NDI along the *z*-direction.

All in all, the newly obtained set of results at the PBE+U-D3(BJ) theory level demonstrate that even when the self-interaction error is considered in the geometry optimization of M(NDIDP) MOFs, configuration-dependent CT properties are found to persist. The actual degrees of band dispersion are dependent on the precise configurations of the MOFs that change with the different levels of theory, which is not unexpected given the results presented in **Figure 6** of main text, where small changes in configuration can still lead to notable differences in the resulting band dispersion. Nonetheless, tunable conduction properties characterized by the transition from 1D to 2D charge transport between the *lp* to *np* phases of M(NDIDP) MOFs are importantly found to be independent of the precise methods used for the geometry optimization calculations. As such, it is concluded that framework flexibility of the M(NDIDP) MOFs effectively leads to the tunable conduction properties in these newly designed MOFs.

***Brillouin Zone Plots for M(NDIDP)-lp and M(NDIDP)-np***

In **Figure S34**, shared below, diagrams for the Brillouin zones of M(NDIDP) in both *lp* and *np* phases are given. Note that since the Brillouin zones are defined in the reciprocal space, path distances are inversely proportional to the real space unit cell dimensions of the MOFs.
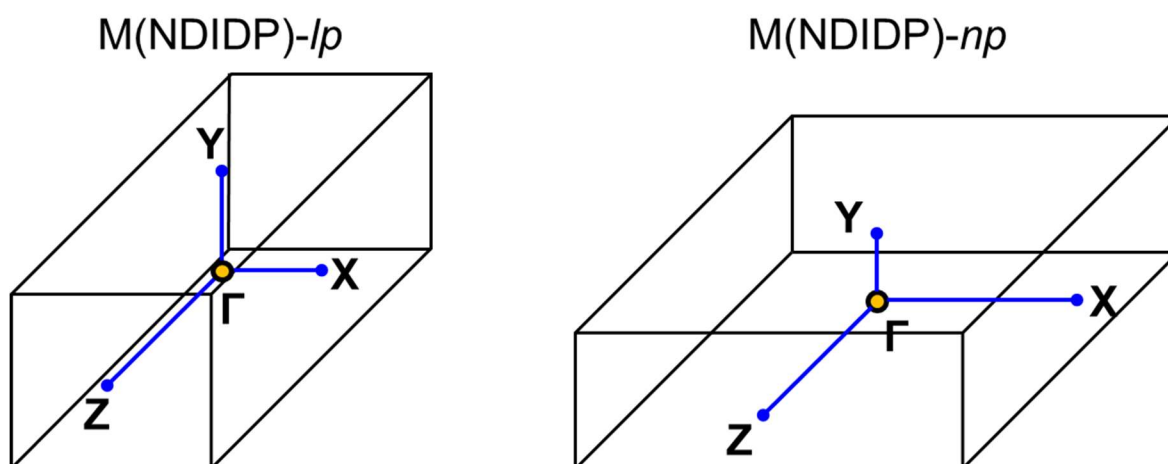


**Figure S34.** Brillouin zone plots for M(NDIDP) in the *lp* and *np* phases.

**Data Availability**

Optimized structural files of M(NDIDP) MOFs at all volumes considered, DFT-derived force field parameters of M(NDIDP), and inputs for QuickFF, Yaff, and VASP calculations are publicly available in the GitHub repository shared below:

https://github.com/SanggyuChong/MOF_flexconduct_supp.git

Additional data presented in this study are available upon reasonable request from the authors.

**References**

(S1)   Manz, T. A. Introducing DDEC6 Atomic Population Analysis: Part 3. Comprehensive Method to Compute Bond Orders. *RSC Adv.* **2017**, *7* (72), 45552–45581.

(S2)   Ruiz, E.; Alemany, P.; Alvarez, S.; Cano, J. Toward the Prediction of Magnetic Coupling in Molecular Systems: Hydroxo- and Alkoxo-Bridged Cu(II) Binuclear Complexes. *J. Am. Chem. Soc.* **1997**, *119* (6), 1297–1303.

(S3)   Ruiz, E.; Rodríguez-Fortea, A.; Tercero, J.; Cauchy, T.; Massobrio, C. Exchange Coupling in Transition-Metal Complexes via Density-Functional Theory: Comparison and Reliability of Different Basis Set Approaches. *J. Chem. Phys.* **2005**, *123* (7), 074102.

(S4)   Aravena, D.; Venegas-Yazigi, D.; Ruiz, E. Exchange Interactions on the Highest-Spin Reported Molecule: The Mixed-Valence $Fe_{42}$ Complex. *Sci. Rep.* **2016**, *6* (1), 23847.

(S5)   Joshi, R. P.; Phillips, J. J.; Mitchell, K. J.; Christou, G.; Jackson, K. A.; Peralta, J. E. Accuracy of Density Functional Theory Methods for the Calculation of Magnetic Exchange Couplings in Binuclear Iron(III) Complexes. *Polyhedron* **2020**, *176*, 114194.

(S6)   Wang, L.; Maxisch, T.; Ceder, G. Oxidation energies of transition metal oxides within the GGA+U framework. *Phys. Rev. B* **2006**, 73, 195107.

(S7)   Puchala, B.; Morgan, D. Atomistic modeling of As diffusion in ZnO. *Phys. Rev. B* **2012**, 85, 064106.